Contents lists available at ScienceDirect

# **Chemical Physics Impact**

journal homepage: www.sciencedirect.com/journal/chemical-physics-impact





# Synthesis of Ce-doped NiFe<sub>2</sub>O<sub>4</sub> nanoparticles and their structural, optical, and magnetic properties

# P. Priyadharshini, K. Pushpanathan

PG and Research Department of Physics, Government Arts College (Autonomous), Karur 639 005 (Affiliated to Bharathidasan University), India

#### ARTICLE INFO

Keywords: Nickel-cerium ferrite Nanoparticles Superparamagnetism Energy gap g-factor

#### ABSTRACT

The impact of Ce<sup>3+</sup> doping on the crystallite size, microstructure, optical, and magnetic characteristics of nickel ferrite magnetic nanoparticles prepared by co-precipitation method is discussed in this article. The x-ray diffractometer, ultraviolet-visible spectrometer, photoluminescence spectrometer, electron paramagnetic resonance spectrometer, and vibrating sample magnetometer were used to characterize the prepared samples. The xray diffraction technique confirmed the cubic phase of all the samples and it further confirmed that the crystallite size steadily reduces from 55.8 to 33.5 nm as the Ce content rises from 0 to 0.15 then it rises to 41.8 nm with Ce content of 0.20. The lattice parameter 'a' was found to increase from 8.3442 to 8.3564 Å with the increase in Ce substitution. As the Ce content increases from 0 to 0.15, the optical band gap increased from 1.50 to 1.95 eV, thereafter, decreasing for Ce content x = 0.20. Fourier transform infrared spectroscopy reveals that the frequency corresponding to the Fe-O vibration of Ce-doped nickel ferrite nanoparticles is pushed towards a shorter wavenumber in contrast to pure nickel ferrite. The spinel structure of the synthesized samples confirmed by the x-ray diffraction pattern was also endorsed by the fourier transform infrared spectra. Photoluminescence spectra confirmed the visible emission from the undoped and Ce-doped nickel ferrite nanoparticles. Transmission electron microscopy analysis confirmed the rectangular shape of the nanoparticles and the reduction in average particle size from 58 to 37.5 nm with an increase in Ce concentration. Energy dispersive x-ray spectroscopy analysis confirmed the presence of Ni, Fe, Ce, and O elements. The explicit magnetic parameters like saturation magnetization, remanence, coercivity, squareness ratio, and magnetic moment were determined from magnetization versus applied field measurements. The result of BET analysis confirmed the porous nature of the Cedoped NiFe<sub>2</sub>O<sub>4</sub> which may be useful in photocatalytic activity. According to magnetic hysteresis curves, the saturation magnetization of nickel ferrite decreases from 51.9 to 22.6 emu/g after Ce content is 0.15. Vibrating sample magnetometer analysis also confirmed the superparamagnetism in nickel ferrite and cerium-doped nickel ferrite samples. Electron paramagnetic resonance confirmed the decrease in spin numbers and the spin relaxation time, after doping with cerium ions.

# 1. Introduction

In recent days, complex metal oxides play critical roles in a variety of chemical and physical processes. Because of their physicochemical properties, they have fascinated the interest of many researchers [1]. There are a large variety of metal oxide nanoparticles such as  $TiO_2$  (titania), ZnO (Zinc Oxide),  $Fe_2O_4$  &  $Fe_2O_3$  (magnetic iron oxides),  $BaTiO_3$  (Barium titanate),  $SrTiO_3$  (Strontium titanate), and  $YBa_2Cu_3O_{7-\delta}$  (123 Superconductor) [2,3]. Due to high stability and biocompatibility, these metal oxides find numerous applications in the field of ceramics, solar cells, lithium-ion batteries, solid-oxide fuel cells, supercapacitors,

transistors, gas sensors, photodetectors, and catalysts. Also, they find a variety of biological applications, including antioxidant, anticancer, anticandidal, and antibacterial therapeutic and diagnostic agents, components of medical implants, and medication delivery [4–11]. For example,  $\text{TiO}_2$  with a bio-compatible surface for cells and their spread is repeatedly used in medical implants, antibacterial, and antibiofilm [12, 13]. Similarly,  $\text{Fe}_2\text{O}_3$  and  $\text{Fe}_2\text{O}_4$  have been described for cell labeling, magnetic resonance imaging, hyperthermia, biosensing, and targeted drug delivery. Likewise, ZnO is well-known for its photocatalytic and antioxidant properties [14–17]. When an external magnetic field is applied to these metal oxides, based on their size, orientation, and the

E-mail address: kpngackr@gmail.com (K. Pushpanathan).

 $<sup>^{\</sup>ast}$  Corresponding author.

number of spin-sublattices, they hold different magnetic fields and different responses [18].

Magnetic metal oxide nanoparticles are of great interest in biomedicine due to their ability to manipulate cells and drugs and to separate or remove cells with an external magnetic field [19,20]. Ferrites are metal oxide magnetic nanoparticles that are useful in many types of electronic devices due to their flexibility, low cost, and exceptional electromagnetic performance over a far-reaching range of frequencies [21]. They are hard, brittle, iron-containing, and generally gray or black and are polycrystalline materials. They are composed of iron oxide and one or more other metals including Mg, Al, Ba, Mn, Cu, Ni, Co, or even Fe itself. The molecular formula of ferrite is described by the term  $AB_2O_4$  (A =  $Ni^{2+}$ ,  $Mn^{2+}$ ,  $Mg^{2+}$ ,  $Cu^{2+}$ ,  $Co^{2+}$  and  $B=Fe_2^{3+}$ ) and they have different crystal structures. Based on their crystal structures, they can be classified into four types, i.e., spinel, hexagonal, garnet, and ortho ferrites. Spinel ferrites are also called cubic ferrites and they are the most widely used family of ferrites. Nickel ferrite (NiFe<sub>2</sub>O<sub>4</sub>) and cobalt ferrite (CoFe<sub>2</sub>O<sub>4</sub>) are examples of spinel ferrite. Hexa ferrites are hexagonal ferromagnetic oxides that are represented by the formula MFe<sub>12</sub>O<sub>19</sub>, where M is an element such as Ba, Pb, or Sr. The oxygen ions in these ferrites have a closely packed hexagonal crystal structure. They have strong coercivity and magneto-crystalline anisotropy [22]. Furthermore, due to its superior chemical stability, coercivity, and oxidation resistance, M-type hexaferrite is widely employed in audio-video recording, automotive, and aerospace industrial applications [23-24]. The effect of bimetallic substitution on the microstructure and magnetic properties of Sr-hexaferrite was investigated by Almessiere et al. [25] and they found that the increase in Y<sup>3+</sup> and Ce<sup>3+</sup> contents diminished the particle size, saturation magnetization, retentivity, and coercivity. The next type of ferrite is garnet ferrite whose chemical formula is M<sub>3</sub>(Fe<sub>5</sub>O<sub>12</sub>) where M is yttrium or a rare-earth ion. Garnets have dodecahedral (12-coordinated) sites in addition to tetrahedral and octahedral sites present in spinels. Hence, net ferrimagnetism is a complicated outcome of antiparallel spin alignment across the three types of sites. Orthoferrites typically form in a deformed perovskite structure of the type AFeO<sub>3</sub>. They possess an orthorhombic crystal structure. Here, A represents one or more rare-earth cations of diamagnetic material. In this structure, Fe ions are coupled to six oxygen anions, resulting in an octahedral structure with the Fe ion in the middle [26]. Diamagnetic cation A exists in the interstitial area between the octahedral structures and is coordinated by 12 oxygen anions. They are used as optical sensors and actuators in optical communications. Lanthanum orthoferrites (LaFeO<sub>3</sub>) and dysprosium orthoferrites (DyFeO<sub>3</sub>) are examples of this class of ferrites [27].

Further, spinel ferrites are classified into normal, inverted, and mixed spinel structures according to their cation distribution. As previously mentioned, ferrite nanoparticles are widely used in permanent magnets, high-density data storage, catalyst, and medication delivery [28]. Instead of the usual spinel structure, ferrite crystals have the inverse spinel structure: B cations occupy (1/8) th of the tetrahedral holes, A cations occupy (1/4) th of the octahedral sites, and B cations occupy the remaining (1/4) th octahedral sites. The bulk material of NiFe<sub>2</sub>O<sub>4</sub> is entirely made up of inverse spinel structures [29]. Moreover, the formula  $[M_{1-\delta}^{2+} Fe_\delta^{3+}][M_\delta^{2+} Fe_{2-\delta}^{3+}]O_4$  allows for a mixed spinel structure of ferrites. Here  $\delta$  represents the degree of inversion.

NiFe<sub>2</sub>O<sub>4</sub>, in general, is a ferrimagnetic material with low conductivity, low saturation magnetization (M<sub>s</sub>), low coercivity (H<sub>c</sub>), moderate eddy current losses, and strong electrochemical stability. Nickel ferrite has 32 O<sup>2-</sup>, 8 Ni<sup>2+</sup>, and 16 Fe<sup>3+</sup> ions in its unit cell. Oxygen ions create 32 octahedral sites (called B-sites) and 64 tetrahedral sites (called A-sites), into which 24 cations can be inserted. Fe<sup>3+</sup> ions fill the entire A site in the inverse spinel structure, while Ni<sup>2+</sup> and Fe<sup>3+</sup> ions share the B site. Ferrimagnetism of nickel ferrite results from the anti-parallel spins of Ni<sup>2+</sup> and Fe<sup>3+</sup> at the B and A sites. Both Ni<sup>2+</sup> and Fe<sup>3+</sup> are capable of exchanging electrons at the octahedral site, which distinguishes them as

unique materials that exhibit superior electrical and magnetic capabilities. The dispersal of cations between the A-site and the B-site is determined by the ionic radii of the dopant ion and cation, and the method of synthesis. As a result, the development of a precise method for the synthesis of ferrite nanoparticles with enhanced properties that are suitable for the manufacturing of a variety of devices is an absolute necessity. It has been demonstrated that nickel ferrite nanoparticles can either exhibit superparamagnetic or ferrimagnetic properties, depending on their size. The NiFe<sub>2</sub>O<sub>4</sub> nanoparticles of size less than 15 nm can act as superparamagnetic [30], and those larger than 15 nm can act as ferrimagnetic material. In ferrites, the O<sub>2</sub> atoms enclose the metal ions, which cause a superexchange interaction between the octahedral and tetrahedral sublattices [31] and this interaction disrupts the magnetic characteristics of ferrites.

Nickel ferrite nanoparticles doped with transition and rare-earth metals are being studied widely by various research groups. Trivalent rare-earth dopants prefer a cubic crystallization system occupying the octahedral sites due to their larger ionic radius. Among the various trivalent rare-earth metal dopants, we have chosen cerium. The reason behind the selection of cerium is that (i) cerium is a nonmagnetic element in the f block having a larger ionic radius (1.14 Å) and exceptional 4f shell electronic configurations [32], (ii) it has two oxidation states, such as +3 and +4, ferrites are extremely sensitive to it, (iii)  $Ce^{3+}$ may replace Fe<sup>3+</sup> ions at octahedral sites so it may cause modification in the crystal structure, optical and magnetic properties [33], (iv) there has been little focus on the bandgap of Ni-Ce ferrites, and (v) the magnetic moment of  $Ce^{3+}$  (2  $\mu B$ ) is greater than  $Fe^{3+}$  (1.73  $\mu B$ ) (vi) Ce has good stability under irradiation and the strong adsorption capacity. Furthermore, the electron exchange that happens in the ferrite structure between the Fe-Fe, Fe-Ni, Fe-Ce, and Ni-Ce cations causes changes in the characteristics of the nanostructured material [34].

Numerous researchers have investigated the effects of various rareearth ions on the coercivity, saturation magnetization, and blocking temperature of NiFe<sub>2</sub>O<sub>4</sub>, Dy<sup>3+</sup> substituted NiFe<sub>2</sub>O<sub>4</sub> nanoparticles [35, 36], Nb<sup>3+</sup>substituted Co<sub>0.5</sub>Ni<sub>0.5</sub>Fe<sub>2</sub>O<sub>4</sub> nanoparticles [37], Eu<sup>3+</sup> substituted Ni-Cu-Zn spinel ferrites [38], Ga<sup>3+</sup>-Gd<sup>3+</sup> ions substituted ternary NiCuZn spinel ferrites [39], La<sup>3+</sup> and Y<sup>3+</sup> ions substituted Ni<sub>0.3</sub>Cu<sub>0.3</sub>Zn<sub>0.4</sub>Fe<sub>2</sub>O<sub>4</sub> nano spinel ferrites [40], However, there has been little focus on the structural, optical and magnetic properties of Ce doped NiFe2O4 ferrites. For instance, Nabi et al. have probed the outcome of Ce substitution on boosting the activity of supercapacitors. They showed that NiCe<sub>0.5</sub>Fe<sub>1.5</sub>O<sub>4</sub> has the largest specific capacitance, boosting electrochemical activity [41]. Similarly, Dixit et al. have explored the physical characteristics of Ce-substituted nickel ferrite nanopowders synthesized by co-precipitation method. After doping with Ce (0.10) they found a decrease in magnetization [42]. Equally, Elayakumar et al. have synthesized NiCeFe<sub>2</sub>O<sub>4</sub> nanopowders through the sol-gel process and investigated their antibacterial and magnetic properties. They observed that the average crystallite size dropped progressively as the Ce concentration increased [43]. In the same way, Dixit et al. have synthesized a sequence of NiCe<sub>x</sub>Fe<sub>2-x</sub>O<sub>4</sub> (x = 0, 0.01, 0.02, 0.03, 0.04, 0.06, 0.08, and 0.10) nanoparticles by a chemical approach and investigated their structural and magnetic properties. Ce substitution lowers the electron paramagnetic linewidth and eddy current fatalities of NiFe<sub>2</sub>O<sub>4</sub> ferrites, according to their experiments [44]. Correspondingly, Maheen et al. have conducted dielectric analyses of NiCeFe<sub>2</sub>O<sub>4</sub> nanoparticles prepared by the sol-gel technique. According to their research, the substitution of Ce<sup>3+</sup> for Fe<sup>3+</sup> decreases the electrical storage capacity of a dielectric material and the loss of tangent [45]. Again, Dixit et al. have studied the effect of annealing on the EPR spectrum of cerium and gadolinium-substituted nickel ferrite nanopowders prepared by chemical route. According to their VSM results, the coercivity and magnetization were lowered after doping with both rare-earth ions [46]. Compatibly, Sonia et al. have explored the effect of lattice straining on the crystal structure, and magnetization of cerium-doped NiFe<sub>2</sub>O<sub>4</sub> nanoparticles synthesized by the sol-gel method.

They found from FTIR data that the insertion of cerium ions resulted in a minor shift in the octahedral absorption band towards the lower frequency side [47]. According to the research that has already been published in this field, it is obvious that Ce-substituted NiFe $_2$ O $_4$  nanoparticles still require some additional examination into their structural, optical, and magnetic capabilities. These intriguing characteristics have motivated us to settle on Ce-doped NiFe $_2$ O $_4$  magnetic nanoparticles as the subject of the present investigation.

According to the findings of recent studies, the shape, size, and nanostructures of ferrites can be precisely controlled by modifying both the composition and the methods of synthesis. In order to successfully synthesize ferrite nanoparticles, numerous methods, such as mechanical milling, sol-gel [48], solid-state, thermal decompositions, hydrothermal [49], a sonochemical method [50], combustion method [51], and co-precipitation methods, have been developed during the course of many years. Of these options, we have chosen the co-precipitation method for the present work. It has the benefit of mixing at the atomic level, resulting in homogeneous smaller particles. The precipitation method is a proven, a relatively simple, large quantity of product that can be obtained at a low cost. This approach also necessitates a low-temperature annealing process to remove defects in the crystallographic planes and minimize internal stresses. Moreover, a process for the synthesis of ferrite nanostructures that is both extremely efficient and accurate is not even close to being developed. This is in addition to the fact that the distribution of Ce<sup>3+</sup> cations inside the NiFe<sub>2</sub>O<sub>4</sub> structure has not been determined clearly.

In response to this requirement, we investigated the effect of Ce doping on the crystallite size, surface morphology, and magnetization behavior of NiCe<sub>x</sub>Fe<sub>2-x</sub>O<sub>4</sub> (x=0.00-0.20, in steps of 0.50) nanopowders synthesized by chemical precipitation method. A variety of analytical techniques were performed to do the in-depth characterization of the samples after annealing them at 800 °C. In addition to this, a relation between the crystal structure and the magnetic properties of the material was found. Inspired by these goals, an endeavor was made to prepare the nanopowders of the NiCe<sub>x</sub>Fe<sub>2-x</sub>O<sub>4</sub> using the cost-effective chemical co-precipitation method. Novelties of the present work are (i) single-domain size of NiFe<sub>2</sub>O<sub>4</sub> may be up to 56 nm, (ii) ferrites with wide energy gap  $\sim 1.95$  eV can be synthesized by co-precipitation method, (iii) non-magnetic Ce reduces the particle size of NiFe<sub>2</sub>O<sub>4</sub>.

#### 2. Experimental procedure

The chemical co-precipitation method was used to synthesize the cerium-doped nickel ferrite nanoparticles that have a nominal composition of NiCe $_{\rm x}$ Fe $_{\rm 2-x}$ O $_{\rm 4}$  (where  $x=0.00,\,0.05,\,0.10,\,0.15,\,$  and 0.20). In this method, each sample was prepared by mixing the intended proportion of precursors. Analytical reagent grade chemicals such as nickel chloride hexahydrate (NiCl $_{\rm 2}$ ·6H $_{\rm 2}$ O, 99% purity), iron (III) chloride tetrahydrate (FeCl $_{\rm 3}$ ·4H $_{\rm 2}$ O, 99% purity), cerium nitrate hexahydrate (Ce (NO $_{\rm 3}$ ) $_{\rm 3}$ ·6H $_{\rm 2}$ O, 99% purity), and sodium hydroxide (NaOH, 99% purity) were used for synthesis without further purification

For the synthesis of NiFe $_2$ O $_4$ , 0.2 M (4.75 g) of NiCl $_2$ ·6H $_2$ O and 0.4 M (6.49 g) of FeCl $_3$ ·4H $_2$ O were mixed in 100 ml double-distilled water at 60 °C. 5 mL of polyethylene glycol (MW 4000) was added over the mixture of metal chlorides solution to act as surfactant agent and to prevent the agglomeration of the product particles. A 3 M NaOH solution was applied drop-by-drop to the mixed solution until the pH of the solution reaches 12, demonstrating the non-existence of metal chlorides in the system. Throughout the synthesis process, a temperature of 80 °C was maintained and vigorous magnetic stirring was continued for 3 h. During this period, the atoms will arrange themselves to form the mixed spinel structure. The solution was then allowed to precipitate at room temperature overnight and then filtered after being repeatedly washed with double-distilled water and ethanol until the pH of the solution fell below 7. The wet precipitate was crushed into nanoparticles of nickel ferrite after being dried at 80 °C in a hot air oven for 10 h to remove the

residual water content. In order to obtain Ce-doped NiFe<sub>2</sub>O<sub>4</sub>, the same procedure was repeated in presence of a needed amount of 0.33 g for x=0.05, 0.65 g for x=0.10, 0.97 g for x=0.15 and 1.33 g for x=0.20 of Ce(NO<sub>3</sub>)<sub>3</sub>·6H<sub>2</sub>O. Finally, all the synthesized nanopowders were annealed at 800 °C for 4 h to acquire the good crystalline character of the sample. The overall chemical reaction involved in the synthesis process is as follows;

$$0.2 \text{ Ni}^{2+} + \text{xCe}^{3+} + (2-\text{x}) \text{ Fe}^{3+} + 40^{2-} \rightarrow \text{Ni}_{0.2}\text{Ce}_{\text{x}}\text{Fe}_{2-\text{x}}\text{O}_4$$

Also, the schematic illustration for the synthesis procedure is shown in Fig. 1.

To examine the crystalline structure of the prepared nanopowders, a Rigaku Ultima-IV x-ray diffractometer operated at 40 kV/30 mA using CuK $\alpha$  radiation of wavelength ( $\lambda$ =1.541 Å) was employed between the diffraction angles 10 and 80. The instrument used a nickel filter, and it scanned the powder samples at the rate of 0.05/min. Optical absorption and transmittance data at room temperature were obtained with a Shimadzu UV-1900i UV-visible-NIR spectrophotometer between the ranges of 190 and 1100 nm. To identify the functional groups contained in the samples, a Fourier Transform Infrared Spectrometer (FTIR: RX1 PerkinElmer) with a potassium bromide beam splitter was employed in the wavenumber range of 4000–400 cm<sup>-1</sup> (resolution: 2 cm<sup>-1</sup>). The photoluminescence spectrometer (Varian Cary Eclipse Fluorescence spectrophotometer) was used to record the luminescence behavior at an irritation wavelength of 330 nm using a He-Cd laser as an irritation source. Microstructure examination was carried out using a JEM-2010 transmission electron microscope operated at 200 kV. The Cu grid sprayed with carbon was utilized to cover the samples for recording the images. A tiny volume of colloidal dispersion was initially diluted in a toluene phase to prepare the samples for morphological investigation. The composition of the samples was analyzed on the JEOL 2010f equipped with an Oxford INCA Energy Dispersive Spectrometer (EDS).

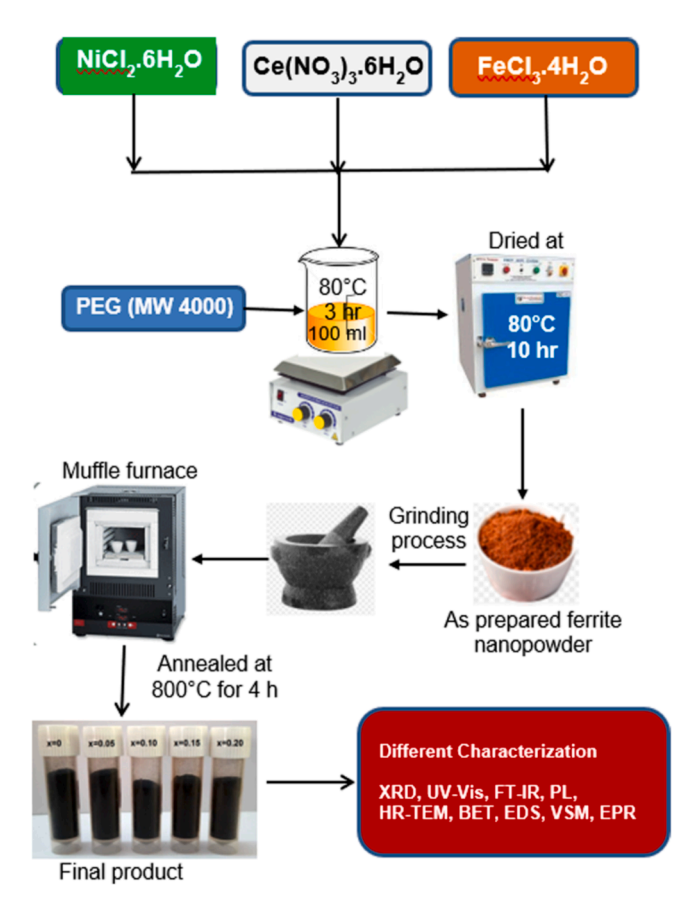


Fig. 1. Schematic illustration of synthesis procedure.

Brunauer, Emmett, and Teller (BET) analysis were performed to determine the specific surface area and pore size distribution of NiFe $_2O_4$  NiCe $_{0.10}$ Fe $_{1.90}O_4$  and NiCe $_{0.20}$ Fe $_{1.80}O_4$  samples using a Gemini VII 2390 surface analyzer (Micromeritics Gemini 2380, USA) at liquid nitrogen temperature using  $N_2$  gas as an adsorbent. The samples were dehydrated at 90 °C for 4 h and then degassed at 300 °C for 2 h before the analysis. The magnetization measurements at room temperature were conducted using a Princeton Micro Mag 2900 vibrating sample magnetometer. With magnetic fields of  $\pm 16$  kOe, the hysteresis curves for samples of undoped and Ce-doped NiFe $_2O_4$  nanoparticles were examined to identify the ferromagnetic/superparamagnetic components. A traditional X-band EPR spectrometer (Bruker model: EMX) fetching a 100 kHz AC magnetic field was used to record the first derivative absorption signal of NiFe $_2O_4$  and Ce-doped NiFe $_2O_4$  nanopowders spread consistently on an adhesive cellulose tape as a thick film.

#### 3. Results and discussion

#### 3.1. X-Ray diffraction analysis

X-ray diffraction (XRD) pattern of the prepared NiCe<sub>x</sub>Fe<sub>2-x</sub>O<sub>4</sub> (x =0-0.20, in steps of 0.50) nanopowders, recorded at room temperature is demonstrated in Fig. 2. Using the X'Pert High Score software, the collected data were processed and then correlated with the standard JCPDS data card 10-0325. The XRD outline of undoped and Ce-doped  $NiFe_2O_4$  nanoparticles demonstrate nine prominent peaks at  $2\theta =$ 21.4°, 35.3°, 41.7°, 43.6°, 50.7°, 55.8°, 67.8°, 73.9°, and 78.8° which corresponds to the (111), (220), (311), (222), (400), (331), (511), (440) and (531) planes, respectively. These Bragg reflections confirmed the formation of single-phase ferrite nanoparticles with FCC structure ( $fd\overline{3}m$ space group). Furthermore, the detection of many diffraction peaks confirmed the polycrystalline nature, and the breadth of the peaks established the nanocrystallite nature of powders. Up to x = 0.20, it is shown that the samples display a pure spinel phase. However, Dixit et al. [42] reported an impurity phase of CeO2 in NiCe0.10Fe1.90O4 nanoparticles. Similarly, Singh et al. [52] found a pure spinel phase in Gd-doped NiGd<sub>0.04</sub>Fe<sub>1.96</sub>O<sub>4</sub> nanoparticles synthesized by the chemical precipitation method. Guragain has synthesized Tb-doped NiTb<sub>0.10-</sub> Fe<sub>1.90</sub>O<sub>4</sub> nanoparticles by sol-gel method [53]. These earlier reports reveal that the solubility of rare-earth ions in the spinel lattice is restricted and that, at a convinced concentration, the contamination phase arises. Existing data on Ce-doped NiFe2O4 are scarce, although previous research has demonstrated that the dissolving capacity depends on the technique of preparation. Therefore, the current investigation revealed that Ce-doped nickel ferrite may be produced via a

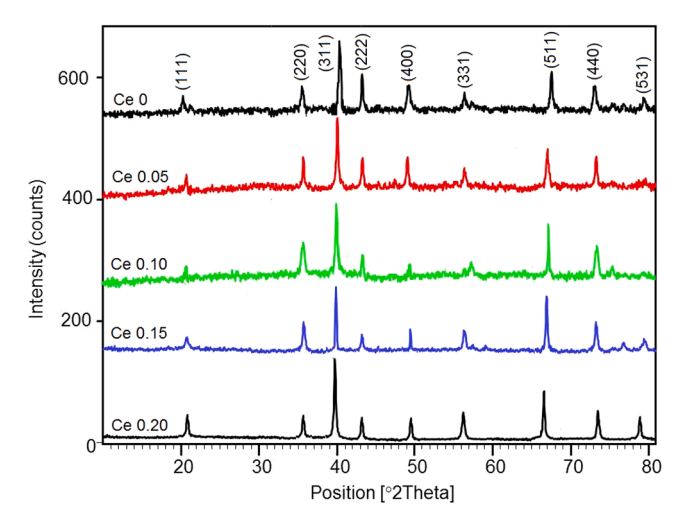


Fig. 2. XRD pattern of synthesized NiCe<sub>x</sub>Fe<sub>2-x</sub>O<sub>4</sub> ferrite nanoparticles.

co-precipitation procedure up to x=0.20, without any impurity phase. Using Scherrer's formula [54] as given in the following equation, the average crystallite size (D) was computed:

$$D = \frac{0.9\lambda}{\beta\cos\theta} \cdot \text{nm} \tag{1}$$

where  $\lambda$  signifies the wavelength of CuK<sub>\alpha</sub> radiation (1.541 Å),  $\beta$  denotes the full width at half maximum (FWHM, in radian), and  $\theta$  denotes the diffraction angle (in radian). The mean crystallite size of NiFe<sub>2</sub>O<sub>4</sub> calculated was noticed to be 55.8 nm. Following doping with a Ce concentration of x = 0.05, the mean crystallite size of the NiCe<sub>0.05</sub>-Fe<sub>1.95</sub>O<sub>4</sub> sample reduces to 42.2 nm. Further, increase in Ce content up to x = 0.15, the crystallite size decreases continuously to 33.5 nm, and then climbs to 41.8 nm when the concentration is increased to x = 0.20; nonetheless, it is however reduced than undoped NiFe2O4 ferrite. Manouchehri et al. [56] reported the average crystallite size of 13 nm for dimercaptosuccinic acid-coated NiFe<sub>2</sub>O<sub>4</sub> nanoparticles. The findings presented here show that the average crystallite size is bigger than those observed by Manouchehri et al. It is interesting to note that the crystallite size does greatly decrease by nearly 22.3 nm (55.8 to 33.5 nm) when x is increased from 0 to 0.15. Nabi et al. [41] observed an analogous tendency of reduction in crystallite size in NiFe<sub>2</sub>O<sub>4</sub>. The rise in crystallite size after x = 0.15 demonstrates that the Ce<sup>3+</sup> ions go to the spinel lattice until x = 0.15, after which they start to settle at the grain boundaries. Doping with a higher percentage of Ce requires a large amount of energy to push the bigger radius Ce (1.14 Å) ion in place of the Fe ion (0.64 Å) and produce the Ce–O bond, resulting in a reduction in the crystallite size. The energy that is necessary for this process is given at the expense of crystallization; as a result, there is a trend toward less crystallinity with decreasing crystallite size [55]. Therefore, a higher amount of Ce doping into the NiFe2O4 lattice limits crystallite growth probably slowing the formation of grain boundaries, and/or modifies the rate of nucleation during sample crystallization, resulting in a reduction in crystallite size.

A rare-earth element can be substituted into NiFe $_2O_4$  to potentially alter the lattice parameter. Since Ce $^{+3}$  ions are larger than Fe $^{3+}$  ions, it is expected that they will fill the B site of the spinel rather than the smaller A site. However, strain is introduced into the lattice because the radius of the Ce ions is larger than the B-site. The following Cullity formula gives the micro-strain ( $\epsilon$ ) as the root-mean-square of the variations in the lattice constant, otherwise known as unit cell dimension [57], between different crystallites.

$$\varepsilon = \frac{\beta \cot \theta}{4} \tag{2}$$

Using the Williamson-Hall (W-H) technique [58], it is possible to quantify both the average crystallite size and the lattice strain, which is a measure of crystal imperfection. The uniform deformation model postulates that the lattice strain will be consistent across the structure and will be unaffected by the orientation of the crystallographic axes. The modification to Debye-Scherrer's formula is given by,

$$\beta \cos \theta = \frac{k\lambda}{D} + 4\varepsilon \sin \theta \tag{3}$$

Estimates of the crystallite size and lattice strain have been obtained by graphing the values of 4 sin0 and  $\beta\cos\theta$  along the x- and y-axes, separately, and then finding a linear fit between the two sets of data. The crystallite size may be determined by finding the intercept of the line that runs down the x-axis, and the slope of the line that corresponds to it provides the micro-strain in the samples that were synthesized. This information can be found in Fig. 3(a–e). It has been found that the crystallite size determined using the W-H method and Scherrer's formula is quite similar to one another and agrees with one another very well. Based on what is shown in Fig. 3(a-e), an increase in the concentration of Ce causes a strain to be tempted in the nanoparticles that varies between  $2.0\times10^{-3}$  and  $2.675\times10^{-3}$  when the Ce content x rises

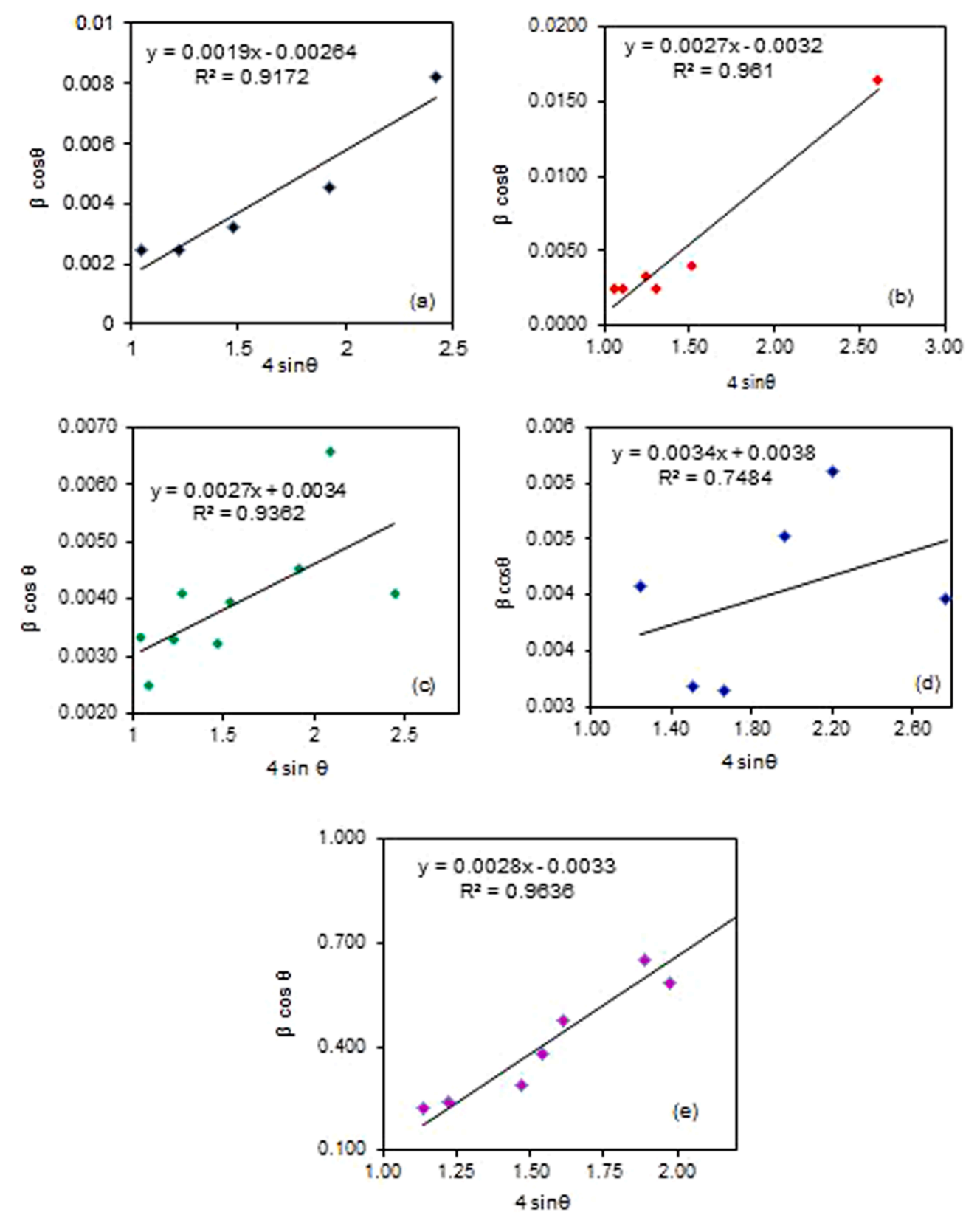


Fig. 3. W-H plots of NiCe<sub>x</sub>Fe<sub>2-x</sub>O<sub>4</sub> ferrite magnetic nanoparticles.

from 0 to 0.20.

Following the incorporation of  $Ce^{3+}$  ions, the XRD pattern reveals that there is a minute movement of the diffraction peaks in the direction of the lower angle. This shift is the result of the incorporation of  $Ce^{3+}$ ,

the ionic radii of which are greater than those of  ${\rm Fe}^{3+}$  (0.65 Å), leading to an increase in the lattice constant of the samples. In addition, the lattice constant (a) was determined by using the following equation,

$$a = \frac{\lambda\sqrt{h^2 + k^2 + l^2}}{2\sin\theta} \tag{4}$$

here, (hkl) represents the crystal plane (311) that was considered for the calculation of crystallite size,  $\theta$  represents Bragg's angle, and  $\lambda$  assumes the wavelength of the x-ray (1.541 Å). From Table 1, it can be shown that the lattice constant rises from 8.3442 to 8.3564 Å when the Ce concentration increases up to 0.15, and then it decreases to 8.3531 for x=0.20. Our observation is just the opposite of Bakeer et al. [59]. They noted a lowering of the lattice constant with an increase in Ce content. Fig. 4 displays the relation between the variation in 'D' and ' $\alpha$ ' for different Ce content. The Nelson-Riley plot was used to calculate the lattice constant with the greatest degree of accuracy. The NR function can be found in,

$$F(\theta) = \frac{1}{2} \left( \frac{\cos^2 \theta}{\sin \theta} + \frac{\cos^2 \theta}{\theta} \right) \tag{5}$$

The Nelson-Riley graph was drawn by putting  $F(\theta)$  on the x-axis and the lattice constant on the y-axis. The exact value of the lattice constant can be found in Fig. 5 by extrapolating the straight-line fit along the y-axis. Calculated from the NR plot, the lattice constant goes from 8.3411 Å to 8.3568 Å, for x=0 to 0.15 in steps of 0.05. After that, the lattice constant goes down, as shown in Table 1. Also, when  $Ce^{3+}$  ions were used instead of  $Fe^{2+}$  ions, the lattice constant gets altered. This may have led to porosity in the ferrite nanoparticles, which was found by calculating the bulk density  $(\rho_b)$  and the x-ray density  $(\rho_x)$ . The bulk density  $(\rho_b)$  was intended using the following equation.

$$\rho_b = \frac{m}{\pi r^2 h} g / cm^3 \tag{6}$$

where m is the mass, r is the radius (0.65 cm) and h is the thickness (1.42 cm) of the pellet and the densities were measured to be 4.0478, 3.9121, 3.7161, 3.4372, and 3.1282 g/cm<sup>3</sup> for x = 0, 0.05, 0.10, 0.15 and 0.20, correspondingly. There was a minor difference in the total mass of the particle, which led to a difference in the bulk density.

The x-ray density  $(\rho_x)$  can be calculated for all forms of material like powder samples, thin films, and bulk materials and it is a prevailing tool for describing materials to study the variations in the crystal structure of the crystalline material. It was estimated after the powder samples were compressed into pellets using an agate mortar and pestle apparatus for 15 min. For making the pellets, the dry powders were mixed in a homogenous manner. The powders were then pelletized using a hydraulic press and 50 kN of force was applied to each pellet for six minutes. Then, they were calcined in a muffle furnace at a temperature of 600 °C for three hours before being gradually cooled down to room temperature.

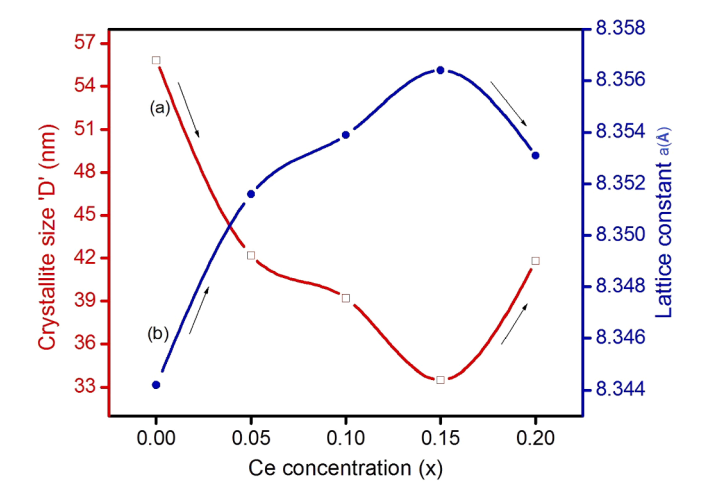


Fig. 4. Correlation between Ce content x, (a) crystallite size 'D', and (b) lattice constant 'a'.

The equation that was used to determine the x-ray density (or) theoretical density from the diffractograms is provided below [60],

$$\rho_x = \frac{8 M}{N_A a^3} \cdot g / \text{cm}^3 \tag{7}$$

where M is the molecular weight (234.62 g/cm<sup>3</sup>) of NiFe<sub>2</sub>O<sub>4</sub>,  $N_A$  is Avogadro's number (6.022 × 10<sup>23</sup>) and  $a^3$  is the unit cell volume of the sample concerned.

The x-ray density ( $\rho_x$ ) has a reciprocal relationship with the unit cell volume. It can be seen in Table 2, that the lattice constant rises with Ce content, and the value of  $\rho_x$  decreases, going from 5.3649 g/cm<sup>3</sup> to 5.3414 g/cm<sup>3</sup>. Table 2 makes it evident that there is a linear relationship between the concentration of Ce and the x-ray density. This relationship should be explained by the fact that the weight of a cerium atom is greater than that of an iron atom. The correlation between Ce content,  $\rho_x$ , and  $\rho_b$  is shown in Fig. 6.

Due to the creation of pores during the calcination process, the bulk density is typically less than the x-ray density, i.e.,  $\rho_b < \rho_x$ . The large difference in the ionic radius of  $\mathrm{Ce}^{3+}$  and  $\mathrm{Ni}^{2+}$  contributes to the increase in x-ray density. Using the empirical equation provided in the following equation, the porosity (P) of ferrite nanoparticles was calculated.

$$P\left(\%\right) = \left(1 - \frac{\rho}{\rho}\right) \times 100 \tag{8}$$

The calculated porosity percentages are 24.4 when x = 0, 28.0 when x = 0.05, 31.0 when x = 0.10, 39.5 when x = 0.15, and 44.7 when x = 0.20. Notable is the fact that both x-ray density, and the bulk density decrease, as  $Ce^{3+}$  concentration increases. Furthermore, the hopping length between magnetic ions in tetrahedral  $(d_A)$  and octahedral  $(d_B)$  sites were calculated with the help of the equation given below,

$$d_{\mathbf{A}} = 0.25a\sqrt{3} \,\,\mathring{\mathbf{A}} \tag{9}$$

$$d_B = 0.25a\sqrt{2} \text{ Å} \tag{10}$$

As the content of  $Ce^{3+}$  ions grows, the hopping distance between magnetic ions decreases till x=0.05, showing that the magnetic ions are attracted to one another. This may be a result of the different ionic radii of  $Ni^{2+}$  and  $Ce^{3+}$  ions.

#### 3.2. Cation distribution

The study of cation dispersion in spinel ferrite provides a wealth of knowledge for the production of materials with desired qualities. Cation distribution denotes the spreading of metal ions at tetrahedral (A) and octahedral (B) sites. The cation distribution in spinel ferrite can be determined by using the Bertaut method and XRD examination. It is determined by comparing experimentally measured diffraction intensities of hypothetical crystal structures to those calculated for a large number of them. The observed intensity ratios are compared to the theoretically calculated intensity ratios in this procedure.

$$I_{hkl} = |F|_{hkl}^2 PL_p \tag{11}$$

where F is the structure factor, P is the multiplicity factor and  $L_p$  is the Lorentz polarization factor which depends only on Bragg's diffraction angle  $(\theta)$ ,

$$L_{p} = \frac{1 + \cos^{2}2\theta}{\sin^{2}\theta \cos 2\theta}$$
 (12)

For a given spinel compound the analyzed sub-lattice expand or contract on varying oxygen parameter (u) until A-site and B-site volume matches the ionic radii of constituent cations. The best information on cation distribution is achieved when comparing experimental and calculated intensity ratios for reflections whose intensities (i) are nearly

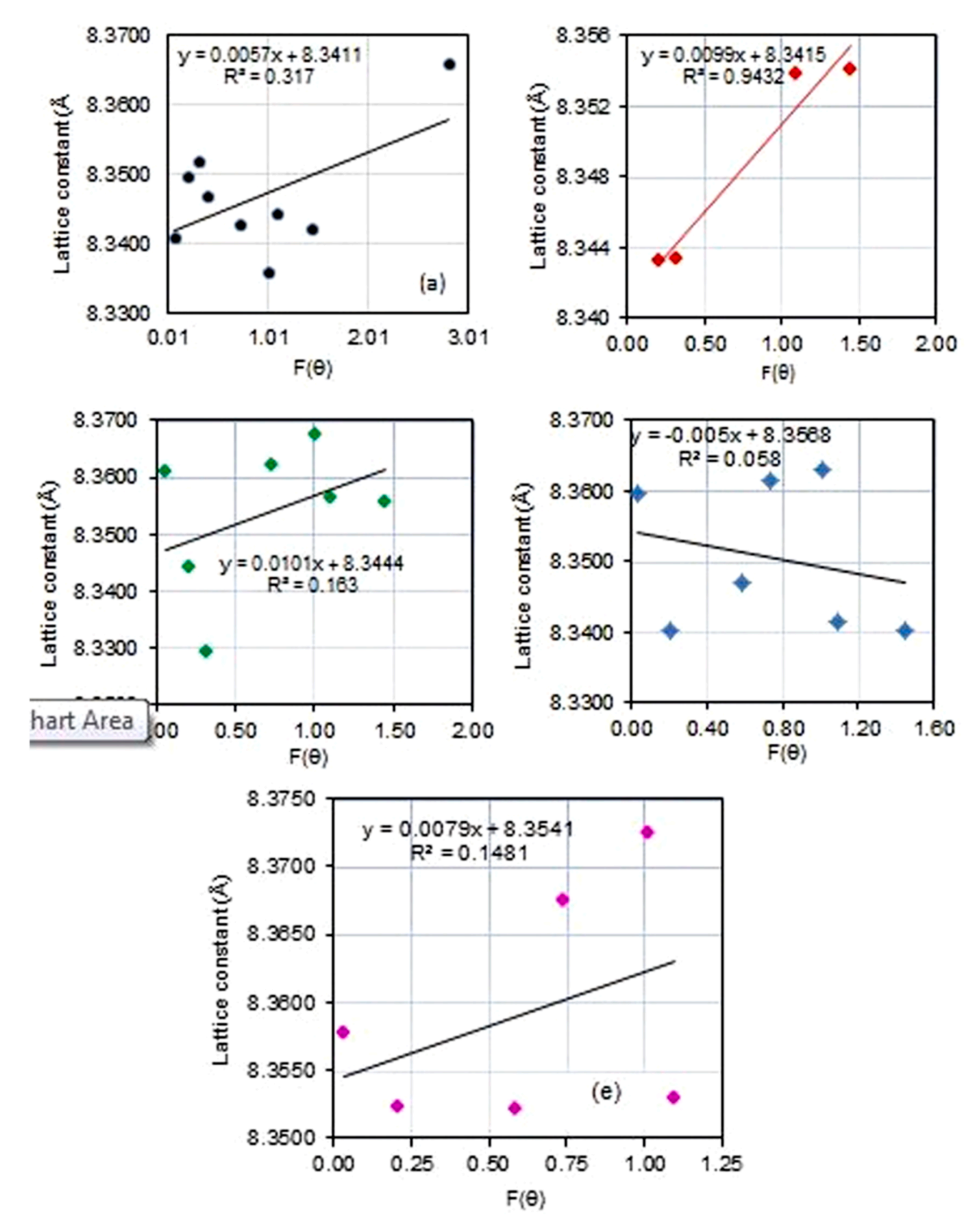


Fig. 5. Nelson-Riley plot of NiCe<sub>x</sub>Fe<sub>2-x</sub>O<sub>4</sub> samples determines lattice constant 'a<sub>o</sub>'.

independent of the oxygen parameter 'u', (ii) in opposite ways vary with the cation distribution and (iii) do not differ significantly. The most suitable reflections are  $(2\ 2\ 0)$ ,  $(4\ 0\ 0)$ , and  $(4\ 4\ 0)$ . In addition, a value of oxygen parameter (u) has to be assumed for the determination of  $I_{cal}$ . In

the NiCe<sub>x</sub>Fe<sub>2-x</sub>O<sub>4</sub> formula, Ni<sup>2+</sup>, Ce<sup>3+</sup>, and Fe<sup>3+</sup> have a strong B-site occupancy, while Ni<sup>2+</sup> and Fe<sup>3+</sup> ions occupy the A-sites. Actually, rareearth metal ion replaces the Fe<sup>3+</sup> ions. The integrated intensities calculated by this method are valid at 0 K. As the observed values are

Table 1 Crystallite size, lattice constant and micro-strain from x-ray diffraction data of NiCe<sub>x</sub>Fe<sub>2-x</sub>O<sub>4</sub> (x = 0, 0.05, 0.10, 0.15, 0.20) nanoparticles.

Ce content (x)	Interplanar Distance $d$ (Å) of (311) plane	Crystallite size (D) nm		Micro-strain (E) x 10 <sup>-3</sup>	Lattice constant calculated from	
		Scherrer method (D) W-H Plot (D')			Experimental (a) Å	Nelson- Riley plot ( $a'$ )Å
0	2.5159	55.8	53.3	2.000	8.3442	8.3411
0.05	2.5181	42.2	43.3	2.669	8.3516	8.3415
0.10	2.5188	39.2	40.8	2.672	8.3539	8.3444
0.15	2.5195	33.5	36.5	3.336	8.3564	8.3568
0.20	2.5186	41.8	42.0	2.675	8.3531	8.3541

Table 2 Dislocation density, the volume of the crystallite, volume of the unit cell, No.of unit cells present in a crystal, x-ray density, and bulk density of the NiCe<sub>x</sub>Fe<sub>2-x</sub>O<sub>4</sub> (x = 0, 0.05, 0.10, 0.15, 0.20) nanoparticles.

Ce content (x)	Dislocation density ( $\delta x 10^{10}$ lines/cm <sup>2</sup> )	Volume of the crystallite (V) $(a')^3 \mathring{A}^3$	Unit cell volume (v) based on $(a')$ $\mathring{A}^3$	No.of unit cells present in a crystal $(V/v)$	X-ray density ' $\rho_x$ ' (g/cm <sup>3</sup> )	Bulk density ' $\rho_b$ ' (g/cm <sup>3</sup> )
0	3.21	79,314,943.2	580.4	136,654	5.3649	4.0478
0.05	5.62	42,524,290.8	580.3	73,277	5.3506	3.9121
0.10	6.51	35,575,734.9	581.5	61,178	5.3462	3.7161
0.15	8.91	25,471,351.2	583.0	43,687	5.3414	3.4372
0.20	3.19	38,808,000.0	583.1	66,554	5.3478	3.1282

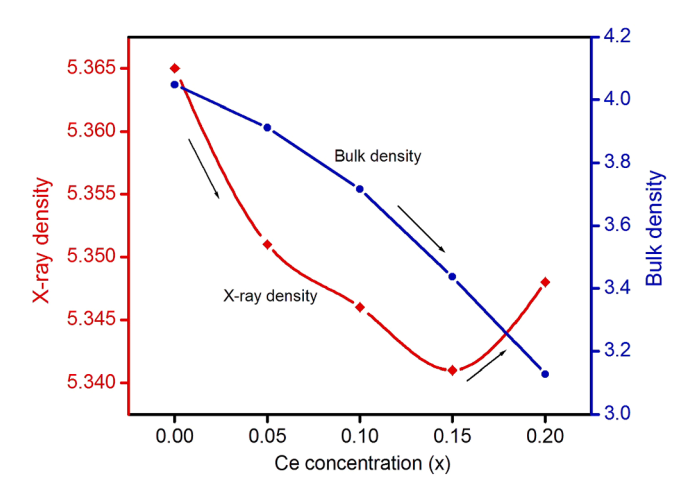


Fig. 6. Variation of x-ray density and bulk density in response to Ce concentration (x).

obtained at room temperature, in principle, a suitable correction is, necessary for precise comparison. However, spinels are high melting compounds; the thermal vibration of the atom at room temperature should not differ substantially from that at absolute zero. Therefore, in our intensity calculation, temperature correction was not necessary. The cation distribution in Ni–Ce ferrite can be represented by,

$$\left(Ni_x^{2+} Fe_y^{3+}\right)_A \left[Ni_{1-x}^{2+} Ce_z^{3+} Fe_{2-(y+z)}^{3+}\right]_B O_4^{2-}$$
(13)

The presence of Ni $^{2+}$ ion in the Ni–Ce ferrite enhances the exchange reaction Ni $^{2+}+Fe^{3+}\leftrightarrow Ni^{3+}+Fe^{2+}$  in octahedral sites, while Ce is preferentially occupied by octahedral sites. This exchange reaction supports the electronic conduction mechanism in Ni–Ce ferrites; the octahedral sites become enlarged when they are occupied by  $Fe^{2+}$  ions instead of Ni $^{2+}$ ions.

The mean cation radius at the tetrahedral A " $r_A$ " and octahedral B site " $r_B$ " was estimated for all samples employing the cation distribution using the above-proposed cation distribution and the following equation.

$$r_{A} = C_{ANi^{2+}} r_{A} (Ni^{2+}) + C_{AFe^{3+}} r_{A} (Fe^{3+})$$
(14)

$$r_{B} \frac{1}{2} \left[ \left( C_{BNi^{2+}} r_{B} (Ni^{2+}) + C_{BCe^{3+}} r_{B} (Ce^{3+}) + C_{BFe^{3+}} r_{B} (Fe^{3+}) \right]$$
 (15)

Where  $C_A$  and  $C_B$  are the ionic concentration at the tetragonal and octahedral sites, respectively, while the ionic radii of  $Ni^{2+}$ ,  $Fe^{3+}$ , and  $Ce^{3+}$  ions in A and B sites are  $r_A(Ni^{2+})=0.55$  Å,  $r_B(Ni^{2+})=0.69$  Å,  $r_A$  ( $Fe^{3+})=0.49$  Å,  $r_B$  ( $Fe^{3+})=0.645$  Å, and  $r_B(Ce^{3+})=1.14$  Å. Table 3 shows results for porosity, SSA, hopping length,  $r_A$ , and  $r_B$  calculations, and Table 4 shows the results of theoritical lattice constant ( $a_{th}$ ), and cation distributions.

Fig. 7 shows the relation between the ionic radius of the A-site ' $r_A$ ' and of the B-site ' $r_B$ ' with Ce<sup>3+</sup> concentration. The decrease in " $r_B$ " may be due to the decreasing amount of Ni<sup>2+</sup> ions from the B-site of larger ionic radii. The increase in " $r_A$ " is due to the increasing amount of larger Ce<sup>3+</sup>ions 1.14 Å to tetrahedral A-site which decreases the smaller Fe<sup>3+</sup> ions 0.67 Å of A-site. The oxygen positional parameter (u) can be calculated using the value of a, the radius of oxygen ion  $R_0 = 1.32$  Å, and  $r_A$  is as follows,

$$u = \left[ (r_A + R_0) \frac{1}{\sqrt{3a}} + \frac{1}{4} \right] \tag{16}$$

The oxygen positional parameter u increases from 0.3856 to 0.3910 Å. The value of the oxygen positional parameter depends on the chemical composition and preparative conditions. In an ideal fcc structure, u=3/8=0.375, for which the arrangement of  $\mathrm{O^{2-}}$  ions equals exactly a cubic closed packing, but in an actual spinel lattice, this ideal pattern is slightly deformed. In the present series, the value of u is much larger, implying that the oxygen ions are displaced in such a way that in the A–B interaction, the distance between A and O ions is increased while that between B and O is decreased. This leads to a decrease in the A-A interaction and an increase in the B-B interaction. Using theoretical expressions discussed elsewhere [61] oxygen positional parameter 'u', tetrahedral and octahedral bond length ( $d_{AX}$  and  $d_{BX}$ ), tetrahedral edge, shared and unshared octahedral edge ( $d_{AXE}$ ,  $d_{BXE}$ , and  $d_{BXEU}$ ) were calculated using the equations given below and the listed in Table 5.

$$d_{AX} = 1.732 \ a[u - 0.25]\mathring{A} \tag{17}$$

$$d_{BX} = a[3u^2 - 2.75u + 0.672]^{1/2} \mathring{A}$$
(18)

$$d_{AXF} = 1.414a[2u - 0.5]\mathring{A}$$
 (19)

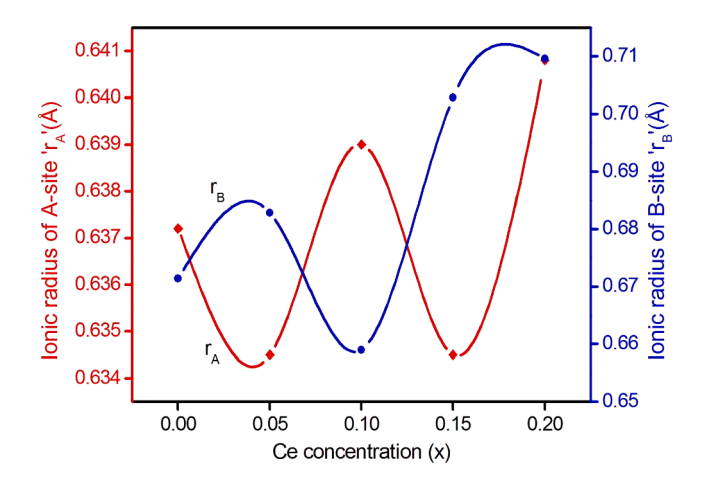
$$d_{BXE} = 1.414 \ a(1-2u)\mathring{A} \tag{20}$$

Table 3 Porosity (P), specific surface area (SSA), hopping lengths of the tetrahedral site ( $d_A$ ) and octahedral site ( $d_B$ ), average ionic radii at A site  $r_A$  (Å) and B site  $r_B$  (Å) in NiCe<sub>x</sub>Fe<sub>2-x</sub>O<sub>4</sub> (x = 0, 0.05, 0.10, 0.15, 0.20) nanoparticles.

Ce content (x)	Porosity (P)%	SSA (m <sup>2</sup> /g)	Hopping lengths (Å) of the	Hopping lengths (Å) of the		Average ionic radii at		
			Tetrahedral site (d <sub>A</sub> )	Octahedral site (d <sub>B</sub> )	A site r <sub>A</sub> (Å)	B site r <sub>B</sub> (Å)		
0	24.4	27.81	3.6118	2.9490	0.6372	0.6714		
0.05	28.0	35.42	3.6120	2.9492	0.6345	0.6828		
0.10	31.0	39.57	3.6132	2.9502	0.6390	0.6590		
0.15	39.5	47.82	3.6186	2.9546	0.6345	0.7028		
0.20	44.7	45.67	3.6174	2.9536	0.6408	0.7096		

**Table 4** Values of  $a_{th}$   $a_{exp}$  and cation distribution of NiCe<sub>x</sub>Fe<sub>2-x</sub>O<sub>4</sub> nanoparticles.

x	u (Å)	$a_{th}$ (Å)	$a_{exp}$ (Å)	Cation distribution
0	0.3856	8.5777	8.3442	$(Ni_{0.05}Fe_{0.95})_A [Ni_{0.95}Fe_{1.05}]_B O_4$
0.05	0.3868	8.6172	8.3516	(Ni <sub>0.07</sub> Fe <sub>0.97</sub> ) <sub>A</sub> [Ni <sub>0.93</sub> Ce <sub>0.05</sub> Fe <sub>0.98</sub> ] <sub>B</sub> O <sub>4</sub>
0.10	0.3883	8.6580	8.3539	$(Ni_{0.15}Fe_{0.93})_A [Ni_{0.85}Ce_{0.10}Fe_{0.97}]_B O_4$
0.15	0.3898	8.6986	8.3564	$(Ni_{0.23}Fe_{0.89})_A [Ni_{0.77}Ce_{0.15}Fe_{0.96}]_B O_4$
0.20	0.3910	8.7383	8.3531	(Ni <sub>0.26</sub> Fe <sub>0.90</sub> ) <sub>A</sub> [Ni <sub>0.74</sub> Ce <sub>0.20</sub> Fe <sub>0.90</sub> ] <sub>B</sub> O <sub>4</sub>



**Fig. 7.** Average ionic radii at A site  $r_A$  and B site  $r_B$  in NiCe<sub>x</sub>Fe<sub>2-x</sub>O<sub>4</sub> (x=0, 0.05, 0.10, 0.15, 0.20) nanoparticles.

 $\label{eq:table 5} \begin{tabular}{ll} \textbf{Summarization of oxygen positional parameter (u), bond length of A-sites ($d_{AX}$) and B-sites ($d_{BX}$), the tetrahedral edge ($d_{AXE}$), the shared and unshared octahedral edges, ($d_{BXE}$ and $d_{BXEU}$) of NiFe_2O_4 samples. \end{tabular}$ 

Ce content (x)	d <sub>AX</sub> (Å)	d <sub>BX</sub> (Å)	d <sub>AXE</sub> (Å)	d <sub>BXE</sub> (Å)	$d_{BXEU}$ (Å)
0	2.9492	3.4582	3.6120	5.4180	5.1081
0.05	2.9490	3.4580	3.6118	5.4177	5.1079
0.10	2.9510	3.4604	3.6143	5.4214	5.1114
0.15	2.9536	3.4634	3.6174	5.4261	5.1158
0.20	2.9537	3.4636	3.6176	5.4263	5.1160

$$d_{BXEU} = a \left[ 4u^2 - 3u + 0.689 \right]^{1/2} \mathring{A}$$
 (21)

A detailed understanding of the above parameters is important because any modification in the structure due to the substitution of a dopant would change the exchange interactions in the spinel lattice, which influences the physical properties of the ferrites. It is noticed that all the constraints are somewhat affected by the substitution of  $\mbox{Ce}^{3+}$  concentration. This may be due to the replacement of larger  $\mbox{Ce}^{3+}$  ions by smaller  $\mbox{Fe}^{3+}$  ions and the constituent ions existing in the corresponding A and B sites.

Here, u oxygen position parameter takes the value of 0.381 Å, 'a' the lattice constant takes the value of 8.5777 Å, and r the oxygen ion ( $O^{2-}$ )

radius takes the value of 1.35 Å. The assessed value of  $d_{AX}$  and  $d_{BX}$  declines as the unit cell dimension lowers until x=0.05, then upsurges as x becomes 0.20. As grain size decreases, the modification in the value of  $d_A$  and  $d_B$  with the unit cell dimension is connected to the distance between magnetic ions. It may also be demonstrated that  $d_A > d_B$ , implying that electron hopping between ions at tetrahedral A and octahedral B sites is less common than between octahedral B sites. Besides, as crystallite size declines, so does the calculated value of  $d_A$ ,  $d_B$ ,  $d_{AX}$ ,  $d_{BX}$ ,  $d_{AXE}$ ,  $d_{BYEL}$ ,  $d_{BYEL}$ ,  $d_{BYEL}$ ,  $d_{BYEL}$ ,  $d_{BYEL}$ ,  $d_{BYEL}$ 

#### 3.3. Confirmation of tetrahedral and octahedral sites by FTIR analysis

The existence of several organic and inorganic molecules in the prepared samples was examined using Fourier transform infrared spectroscopy (FTIR). Typical FTIR spectra of  $NiCe_xFe_{2-x}O_4$  (x = 0.00-0.20, in steps of 0.5) nanoparticles are displayed in Fig. 8. The wide band witnessed around 3390 cm<sup>-1</sup> and 1630 cm<sup>-1</sup> signifies the stretching and bending vibrations of the O—H group. The appearance of the peaks indicates that water molecules are absorbed by the powder samples from the atmosphere while making the pellets with KBr. A stretching vibration occurs when there is a continuous shift in the interatomic distance along the axis of a connection between two atoms. A bending vibration is a shift in the angle that occurs between two bonds. There are four types of bending vibrations: wagging, twisting, rocking, and scissoring. When x is increased to 0.10, these bands are somewhat moved to 3425 cm<sup>-1</sup> and 1631 cm<sup>-1</sup>, frequencies. The existence of C—H stretching vibrations is responsible for the presence of a faint band at 2906 to 2923 cm<sup>-1</sup> [62]. A C=O bond may also be seen in the band at  $1703-1710 \text{ cm}^{-1}$ . From the peak of about  $1362-1386 \text{ cm}^{-1}$ , the anti-symmetric stretching vibration of the COO<sup>-</sup> bond can be seen. The presence of the C—O group can be seen in vibrations between 1022 and  $1047 \text{ cm}^{-1}$  [63]. The bands seen between 1000 and 400 cm<sup>-1</sup> signify metal ion vibrations in the crystal lattice. There are two primary

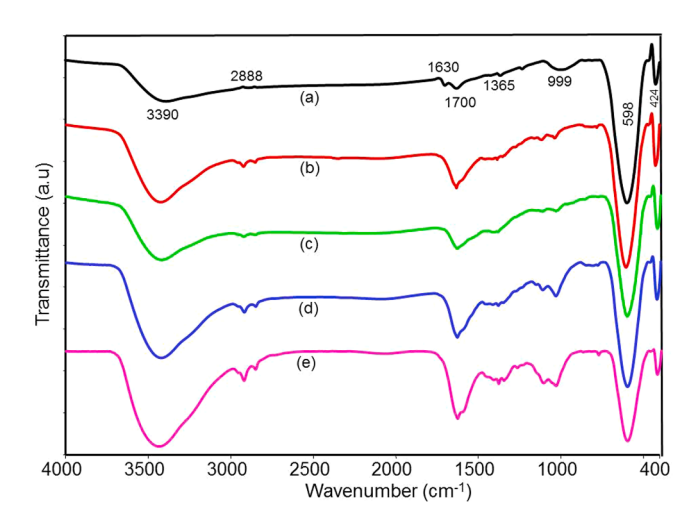


**Fig. 8.** FTIR spectra of the synthesized NiCe<sub>x</sub>Fe<sub>2-x</sub>O<sub>4</sub> nanoparticles; (a) x=0, (b) x=0.05, (c) x=0.10, (d) x=0.15 and (e) x=0.20.

bands in the case of ferrite nanoparticles: the highest one  $(\upsilon_1)$  is about 598–603 cm $^{-1}$  and the lowest one  $(\upsilon_2)$  is about 424–420 cm $^{-1}$ , which correspond to the key stretching vibrations of the metal-oxygen bond in the tetrahedral and octahedral sites, correspondingly [64]. The stretching frequency varies inversely with the atomic weight of the chemical elements present in the samples. This is due to metal ion exchange in the octahedral (Ni<sup>2+</sup> and Fe<sup>3+</sup>) and tetrahedral (Fe<sup>3+</sup>) positions. This demonstrates the replacement of Fe<sup>3+</sup> ions in the octahedral position with Ce<sup>3+</sup> ions. The FTIR spectra thus confirm the formation of the inverse spinel cubic structure. The following formula was used to compute the force constant (k) between Fe<sup>3+</sup> and O<sup>2-</sup> in tetrahedral (F<sub>t</sub>) and octahedral (F<sub>0</sub>) sites.

$$k = 4\pi^2 c^2 v^2 m (22)$$

The force constant of the tetrahedral site is calculated to be in the range of  $2.4493\times10^5$  dynes/cm to  $2.4904\times10^5$  dynes/cm, while the force constant of the octahedral site is found to be in the range of  $1.2313\times10^5$  dynes/cm to  $1.2082\times10^5$  dynes/cm and is mentioned in Table 6. It can be argued that the strength of the metal–oxygen bond is always stronger at the tetrahedral site than at the octahedral site. The existence of functional groups other than metal–oxygen bonds during spectroscopic research is attributable to the absorbance of molecules in the open air and the KBr pellet approach.

#### 3.4. Estimation of the energy gap of Ce-doped NiFe2O4

Optical absorption spectra of  $NiCe_xFe_{2-x}O_4$  (x = 0-0.20, in steps of 0.05) nanopowders recorded at room temperature are displayed in Fig. 9. From which the energy gap  $(E_g)$  of them can be calculated. It can be seen that the cut-off wavelength ( $\lambda_c$ ) is established to be approximately 829 nm for x = 0 and they were shifted to 712 for x = 0.05, 650for x = 0.10, 634 for x = 0.15, and then red-shifted to 661 nm for x =0.20. The corresponding energy gap  $(E_g)$  calculated using the relation  $E_g$  $= (hc/\lambda_c)$  was found to be 1.50, 1.74, 1.91, 1.96, and 1.88 eV for x = 0, 0.05, 0.10, 0.15 and 0.20, respectively. Noticed that the energy gap has been widened till x = 0.15, which implies that the replacement of Fe by Ce broadens the  $E_g$  of NiFe<sub>2</sub>O<sub>4</sub> nanoparticles intensely and a fast-blue shift is observed. Because Ce doping reduces the crystallite size, the  $E_{\sigma}$ broadens due to the quantum size effect. This rise could be attributed to magnetic ion interactions. A similar increase in  $E_g$  has already been reported by Korkmaz et al. [65] and Slimani et al. [66] in NiV<sub>x</sub>Fe<sub>2-x</sub>O<sub>4</sub> nanoferrites. The narrowing of the energy gap of NiFe2O4 with further Ce doping (x = 0.20) is related to the increase in crystallite size and transition tail width.

To better comprehend the change in optical performance resulting from the substitution of Ce, the optical band gap was further investigated by means of Tauc's plot.  $NiFe_2O_4$  is a material with a direct band gap and follows the form [67]

$$(\alpha h v)^2 = B(h v - E_g) \tag{23}$$

 $h\nu$  represents the energy of the input photon,  $\alpha$  is the absorption coefficient, B represents the absorption edge width parameters, and  $E_g$  is the band gap of the samples under study.

Fig. 10(a–e) shows the  $(\alpha hv)^2$  in the y-axis against hv in the x-axis curves of prepared NiCe<sub>x</sub>Fe<sub>2-x</sub>O<sub>4</sub> (x=0–0.20, insteps of 0.5)

**Table 6**Calculation of force constant from FTIR analysis.

Ce content 'x'	$(cm^{-1})$	$(cm^{-1})$	$F_{t}$ ( $\times~10^{5}$ dynes/ cm)	$F_{o}$ ( $\times$ $10^{5}$ dynes/ cm)
0	598	424	2.4493	1.2313
0.05	598	424	2.4493	1.2313
0.10	600	421	2.4657	1.2139
0.15	602	421	2.4822	1.2139
0.20	603	420	2.4904	1.2082

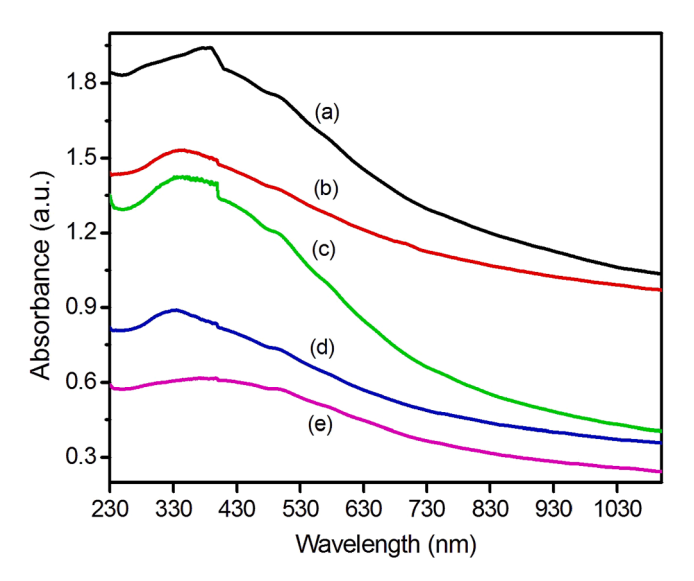


**Fig. 9.** UV–vis absorption spectrum of NiCe<sub>x</sub>Fe<sub>2-x</sub>O<sub>4</sub> ferrite nanoparticles; (a) x = 0, (b) x = 0.05, (c) x = 0.10, (d) x = 0.15 and (e) x = 0.20.

nanoparticles. The values in places with high absorption were fitted with linear regression. The resulting graph consists of a varied linear segment that represents the beginning of absorption. Therefore, the energy gap of the nanomaterial was determined by superimposing the linear section of the graph onto the x-axis using a straight line. The energy gap obtained from the graph was 1.52, 1.75, 1.90, 1.95, and 1.87 eV for NiFe<sub>2</sub>O<sub>4</sub> samples with Ce content x = 0,0.05,0.10, 0.15, and 0.20, respectively. The energy gap observed from Tauc's plot and that computed from the UV-vis absorption spectra are nearly identical. Evidently, the band gap increases as the Ce concentration rises, from 1.52 eV to 1.95 eV. Our NiFe<sub>2</sub>O<sub>4</sub> nanoparticles have a direct band gap of 1.52 eV, which is lower than that of the reported values of 2.5 eV for NiFe<sub>2</sub>O<sub>4</sub> nanoparticles and 2.7 eV for NiFe<sub>2</sub>O<sub>4</sub> films [68,69]. Like the obtained finding in Sn-substituted NiFe<sub>2</sub>O<sub>4</sub> [70] and in Gd-doped NiFe<sub>2</sub>O<sub>4</sub> [71], the growing trend of the optical band gap can be attributed to the reduction of crystallite size.

The following is the mechanism behind the increase in  $E_g$ : The bandgap is the electron's prohibited zone. The valence band and conduction band in ferrite nanoparticles are created by the O-2p orbital and the Fe-3d orbital, respectively. In bulk materials, the band structures are made up of the energy states of many atoms and molecules that are close to each other. But at the nanoscale, there are not as many atoms or molecules as there are in bulk matter, so the energy levels are higher, and the band is wider. This makes the difference in energy between the valence band and the conduction band wider. Hence, we can figure out why the energy gap of the nanoparticle is wider than its bulk matter. The widening of the bandgap suggests that there may not be any more bands between O-2p and Fe-3d This could be because the nanoparticles have a lot of defects on their surfaces and at their interfaces.

#### 3.5. Photoluminescence (PL) study

Photoluminescence spectroscopy is a great way to find out useful information about energy and the movement of charge carriers that are made when light hits something. Electrons can be found in trap states, excitonic states, and conduction bands in spinel ferrites. It is well known that the surface of nanoparticles has a lot to do with how they emit and perform. Because there is an energy gap, surface states come from non-stoichiometric surfaces and bonds that are not fully filled [72]. Surface trap states allow recombination that doesn't involve radiation and improve the efficiency of luminescence. The rate at which electrons and holes come back together is shown by the PL spectrum.

Fig. 11 is a typical PL spectrum of NiCe<sub>x</sub>Fe<sub>2-x</sub>O<sub>4</sub> nanoparticles (x =

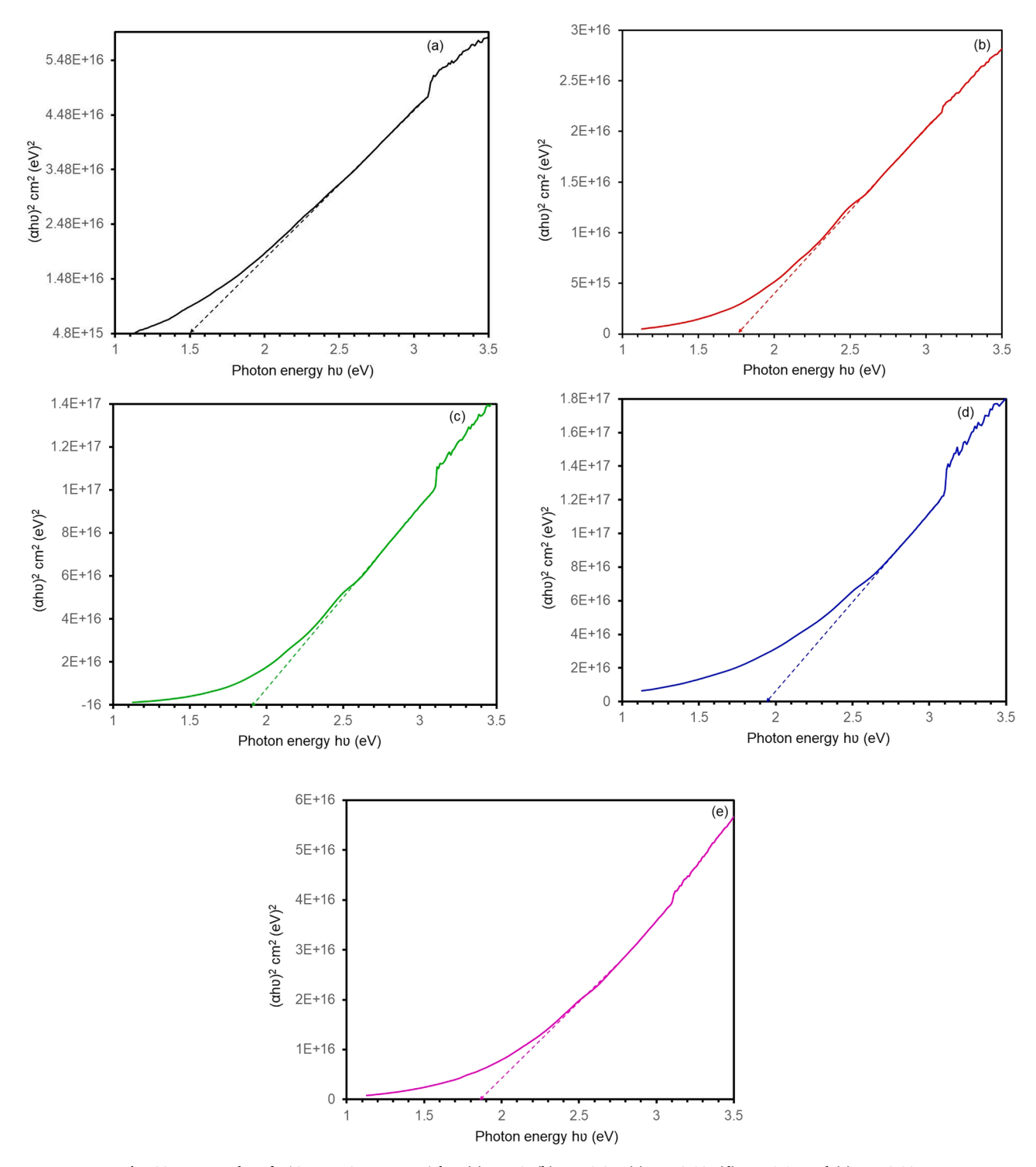


**Fig. 10.** Tauc's plot of NiCe<sub>x</sub>Fe<sub>2-x</sub>O<sub>4</sub> nanoparticles; (a) x = 0, (b) x = 0.05, (c) x = 0.10, (d) x = 0.15 and (e) x = 0.20.

0–0.20, in steps of 0.5) that were excited with a 350 nm laser beam. The PL spectra of the magnetic nanoparticles used in this study consist of two bands, one in the wavelength range of 397 nm, and the other at 705 nm. A less intense emission observed at 397 nm corresponds to the violet emission. It is reported that the violet emission is associated with deep levels such as  ${\rm Fe}^{2+}$  vacancies,  ${\rm O}^{2-}$  interstitials, and dislocations. Surface defect states such as oxygen vacancies located at the surface of Ce-doped NiFe<sub>2</sub>O<sub>4</sub> nanoparticles are the origin of this violet emission. Red emission is the name given to the narrow visible emission that may be observed at a wavelength of about 705 nm. This emission is caused by interstitial defects in the Ni atom. This emission can be traced back to

the recombination of electrons that have been profoundly trapped by oxygen vacancies with holes that have been created during photogeneration. It is common knowledge that spinel ferrite, which is made up of NiFe<sub>2</sub>O<sub>4</sub>, has strong absorption in the ultraviolet-visible spectrum. It is possible to attribute the development of new electronic energy levels between the valence band and the conduction band to the fact that the concentration of  $Ce^{3+}$  is raised. This leads to an overall rise in the intensity of the PL peak for the samples with Ce content x=0.15 which results in the development of new electronic energy levels between the valence band and the conduction band. In UV–visible spectra, we observed a minor shift in peak location, however, in PL spectra, no such

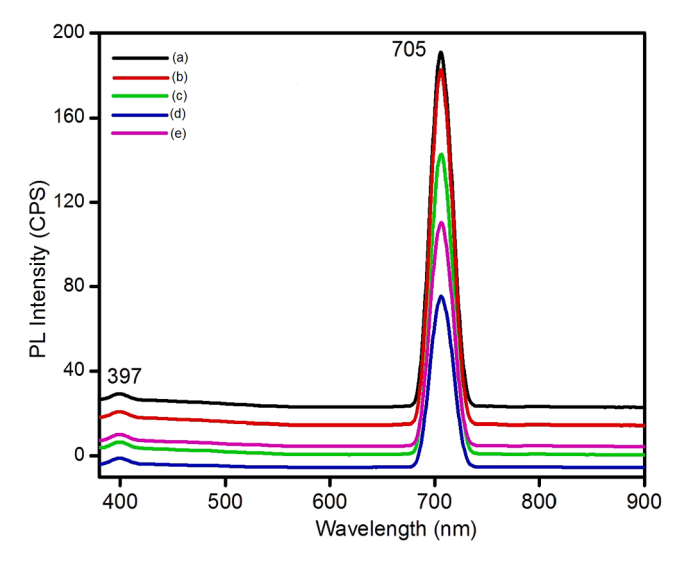


**Fig. 11.** Photoluminescence spectra of the NiCe<sub>x</sub>Fe<sub>2-x</sub>O<sub>4</sub> nanoparticles; (a) x = 0, (b) x = 0.05, (c) x = 0.10, (d) x = 0.15 and (e) x = 0.20.

shift was seen. It suggests that the energy level of defect states and oxygen vacancies in the vicinity of the valance band is nearly constant. It may be the result of larger particles with a smaller surface area. Furthermore, it is thought that the decrease in crystallite size due to the Ce doping creates fewer luminescent centers near the surface than in the interiors, and therefore, the Ce-doped samples have lower emission efficiencies than the undoped NiFe<sub>2</sub>O<sub>4</sub> nanoparticles. The decreased recombination rate may also be a contributing factor to the declined peak intensity of the Ce-doped sample. Visible emissions including blue, green, and red have been confirmed by many research groups in NiFe<sub>2</sub>O<sub>4</sub> nanoparticles [73–75]. We also previously observed a comparable red emission in NiFe<sub>2</sub>O<sub>4</sub> and Ni-doped CoFe<sub>2</sub>O<sub>4</sub> ferrite nanoparticles [76, 77]. Thus, the present PL analysis confirmed that magnetic nanoparticles of NiCe<sub>x</sub>Fe<sub>2-x</sub>O<sub>4</sub> ferrite can emit red light and may be used for optoelectronic devices.

#### 3.6. Microstructural and compositional analysis by TEM and EDS

The particle size and microstructure of the  $NiCe_xFe_{2-x}O_4$  nanoparticles (x=0,0.10, and 0.20) were analyzed using TEM and the results are displayed in Figs. 12, 13, and 14, respectively. Image J free software was used to calculate the particle size, and interplanar spacing and to

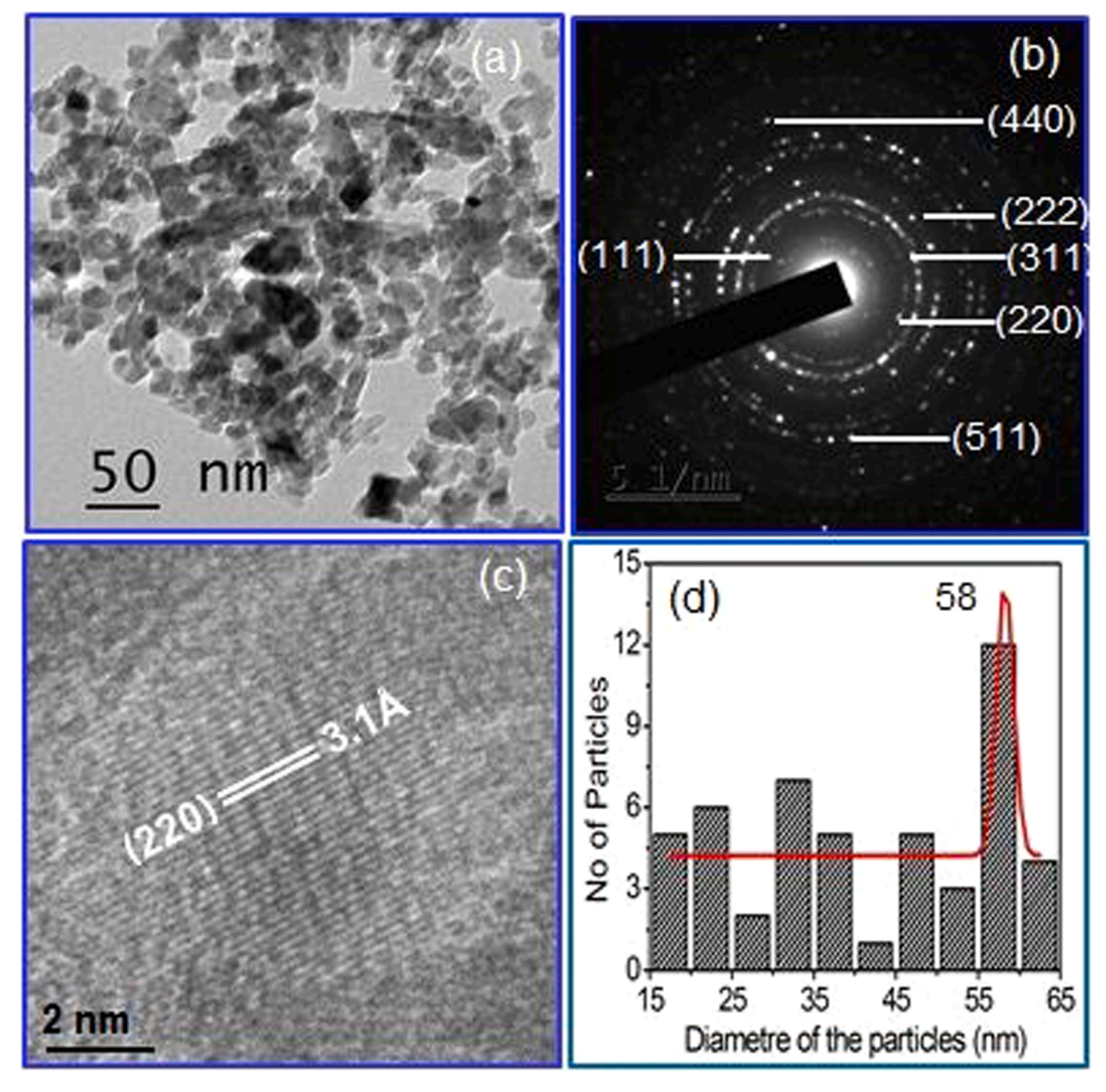


Fig. 12. (a) HR-TEM image (b) SAED pattern (c) lattice fringe width pattern and (d) particle size distribution curve of NiFe<sub>2</sub>O<sub>4</sub> sample.

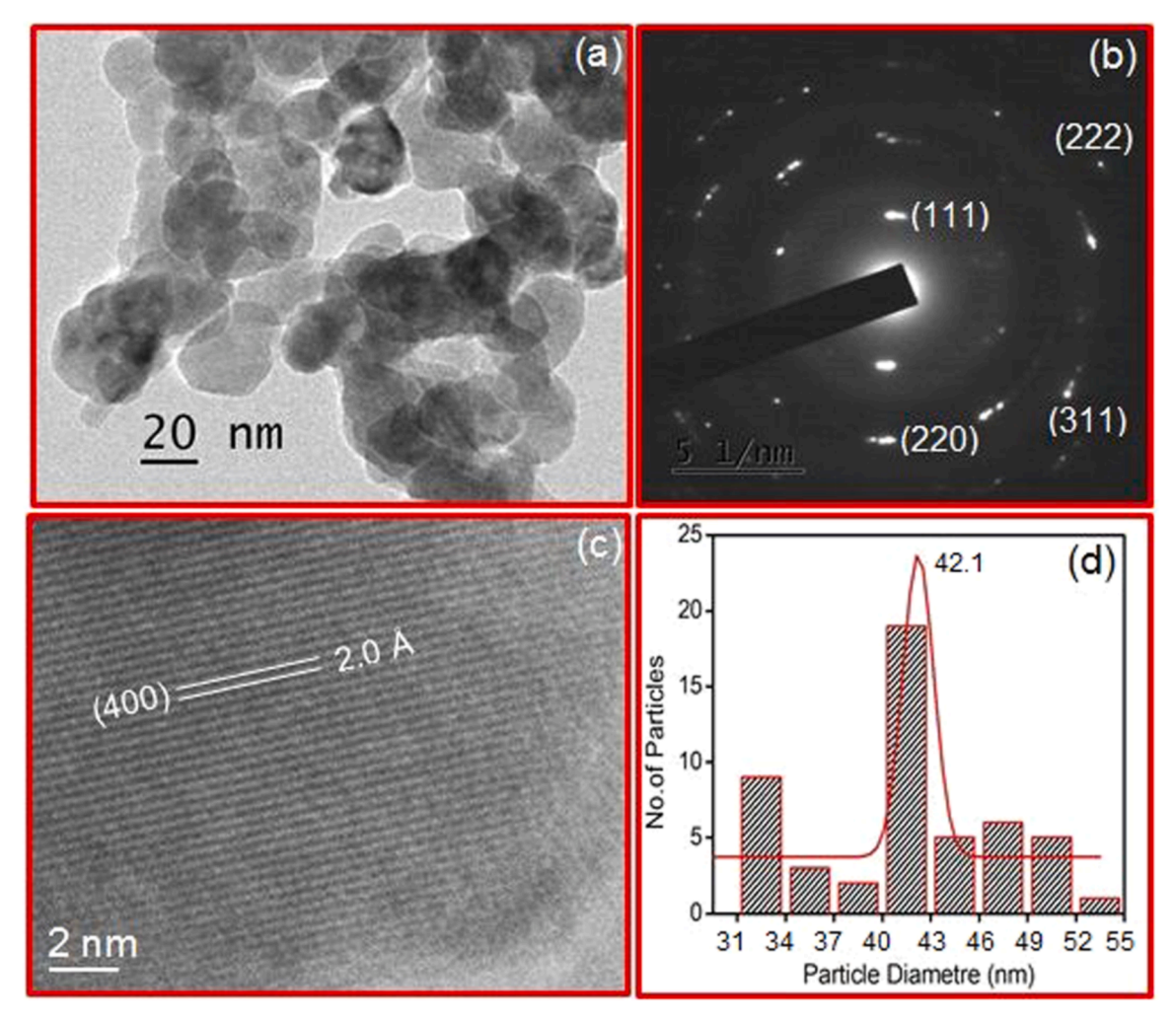


Fig. 13. (a) HR-TEM image (b) SAED pattern (c) lattice fringe width pattern and (d) particle size distribution curve of  $NiCe_{0.10}Fe_{1.90}O_4$  sample.

index the selected area electron diffraction pattern (SAED). It can be spotted from Fig. 12 that the undoped nickel ferrite sample consists of merely uniform size square-shaped aggregated nanoparticles. The particle size distribution curve reveals the particle size distributions are in the range of 15-65 nm with a mean value of 58 nm. NiFe<sub>2</sub>O<sub>4</sub> is an inverse spinel structure in which divalent Ni<sup>2+</sup> ions occupy the octahedral sites and trivalent Fe<sup>3+</sup> ions are distributed among the tetrahedral and octahedral sites. When NiFe2O4 is doped with Ce, results in NiCeFe2O4 which is also inverse spinel, Ce3+ ions replace some Fe3+ from the octahedral sites, depending on the ratio, accordingly, changing the surface morphology and reactivity. When Ce<sup>3+</sup> was added, square shape particles were transformed into nearly spherical shapes as shown in Fig. 13. These exhibit a wide range of particle sizes and almost elongated spherical nanoparticles. Therefore, the root mean square grain size from at least 50 particles has been calculated using the mean square estimation. The average diameter of these spherical nanoparticles is decreasing to 42.1 nm with increasing  $Ce^{3+}$  content x to 0.10. In this case, the particle size distribution is in the range of 32–55 nm. Especially, when x = 0.15, smaller nanoparticles with elongated spherical shapes can be found in Fig. 14. These particles were severely aggregated by nanosized particles. These nanoparticles may be created by magnetic properties. This indicates that Ce declines the grain development till x = 0.15 in the spinel phase NiFe<sub>2</sub>O<sub>4</sub> preparation procedure. It can be considered that while increasing Ce<sup>3+</sup>, the excess Ce<sup>3+</sup> may reside in grain boundaries and constrain grain growth. The decrease in grain boundary produces a loss in surface energy, resulting in weak interactions between particles that cause a minor agglomeration [78]. This causes the shape to change

from square to distorted spherical nanoparticles and the average particle size to decrease to 37.5 nm. Thus, the addition of Ce<sup>3+</sup> to NiFe<sub>2</sub>O<sub>4</sub> played a significant role in the microstructural reformation from a square shape to an elliptical shape [41]. Ce doping into NiFe<sub>2</sub>O<sub>4</sub> nanoparticles is believed to have inhibited the formation of nickel ferrite crystals. As per the reaction-induced grain growth impairment mechanism outlined by Kools [79], doping Ce element into the interior of the NiFe<sub>2</sub>O<sub>4</sub> lattice reduces free energy, hence inhibiting grain growth. This reveals that Ce doping not only influences the surface activity of NiFe2O4 grains but also the condition of grain development; this behavior has been described in XRD. Further, dislocations and stacking faults are not visible in the images of any of the samples. The particle size of all the samples reported here is slightly lower than that of the crystallite size measured by XRD. The XRD provides the mean grain size. Also, XRD determines the crystallinity of the nanoparticles. In contrast, the TEM images reveal the total morphological size of the nanoparticles. Consequently, there is a disparity between the sizes calculated by these two methods. The SAED pattern, which can be seen right away from the bright spots, showed that the nanoparticles were polycrystalline. The bright spots, in the shape of a circle, were used to make indexing the pattern. All the samples are polycrystalline because they all form a ring pattern with dots going in different directions. Some of the bright spots were found to be on the (111), (220), (311), (222), (511), and (440) planes. The fringe width pattern shows that the nanoparticles are crystalline, and the interplanar spacing 3.1 Å, 2.0 Å, 2.4 Å is remarkably close to an interplanar spacing of (220), (400), and (222) planes, respectively, and what was found in JCPDS data card 10-0325.

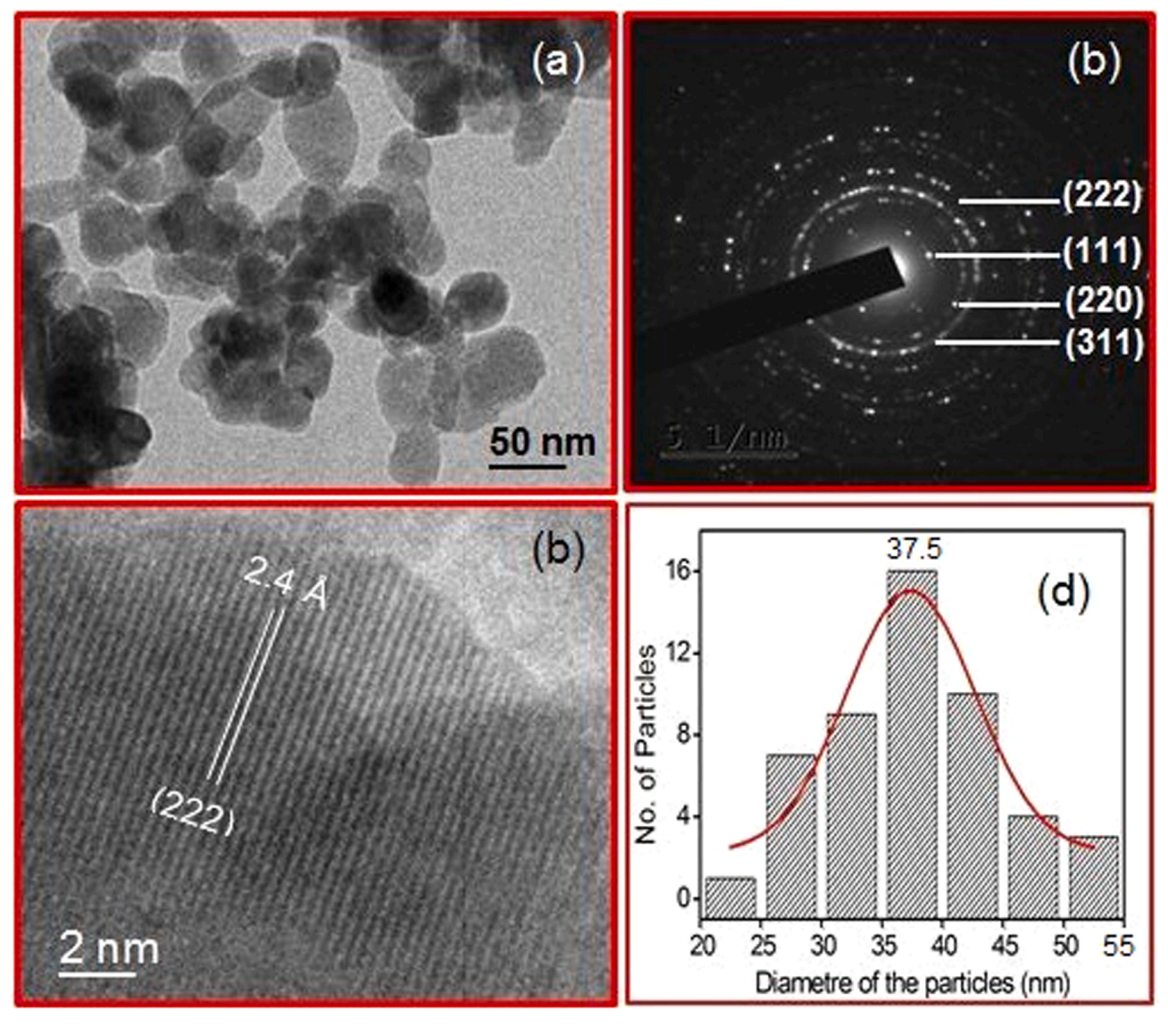


Fig. 14. (a) HR-TEM image (b) SAED pattern (c) lattice fringe width pattern and (d) particle size distribution curve of NiCe<sub>0.20</sub>Fe<sub>1.80</sub>O<sub>4</sub> sample.

EDS was used to determine the chemical composition of NiCe<sub>x</sub>Fe<sub>2-x</sub>O<sub>4</sub> nanoparticles with x values of 0, 0.05, 0.10, 0.15, and 0.20. The results of this analysis are summarized in Table 7, which also shows that the nanoparticles contain the elements Ni, Ce, Fe, and O. The weight percentages of Ni, Ce, Fe, and O found in NiCe<sub>0.15</sub>Fe<sub>1.85</sub>O<sub>4</sub> sample are 11.22%, 13.71%, 21.80%, and 53.90%, correspondingly. Therefore, the compositional analysis verified that the relevant amounts of Ni and Ce ions are present in the NiCe<sub>x</sub>Fe<sub>2-x</sub>O<sub>4</sub> nanoparticles. The components of the sample were selected so that they would be representative of the nominal ones. The EDS spectrum was obtained for each sample, but only the result of the NiCe<sub>0.15</sub>Fe<sub>1.85</sub>O<sub>4</sub> sample is presented in Fig. 15 for illustrative purposes.

#### 3.7. BET analysis

BET analysis is a systematic analysis employed for determining the

specific surface areas and pore size distributions of powder materials. This technique uses the physical adsorption of nitrogen, on the surface of the powder sample. In BET analysis, normally the samples are loaded in an evacuated sample tube and the sample is cooled to cryogenic temperatures before passing an analytical gas at a sequence of accurately controlled pressures. The number of gas molecules adsorbed on the surface increases with increasing pressure. By comparing the equilibrated pressure (P) to the saturation pressure (Po), the relative pressure ratio (P/Po) is calculated, as well as the amount of gas adsorbed by the sample at each equilibrated pressure.

In order to study the adsorption mechanism of the synthesized samples, the  $N_2$  adsorption–desorption isotherm for the  $NiCe_xFe_{2\cdot x}O_4$  (x  $=0.00,\ 0.10,\ and\ 0.20)$  samples were recorded and displayed here. Fig. 16(a) signifies type III isotherm of NiFe<sub>2</sub>O<sub>4</sub> nanoparticles which was accompanied by a hysteresis loop with negligible loss revealing that the sample contains a non-porous surface or macroporous that interacts

**Table 7**Result of chemical analysis of NiCe<sub>x</sub>Fe<sub>2-x</sub>O<sub>4</sub> nanoparticles studied using EDS.

Nominal Cerium content (x)%		Elements i	n (wt%)		Elements in (at%)				Total (%)
	Ni	Ce	Fe	0	Ni	Ce	Fe	О	
0	12.24	0.00	23.22	64.54	4.48	0.00	8.93	86.60	100
5	13.81	4.10	23.82	58.27	5.43	0.68	9.84	84.05	100
10	11.91	7.52	31.97	48.60	5.25	1.39	14.81	78.56	100
15	11.22	13.71	21.80	53.90	4.72	2.42	9.64	83.22	100
20	11.26	13.56	20.24	54.94	4.70	2.37	8.87	84.06	100

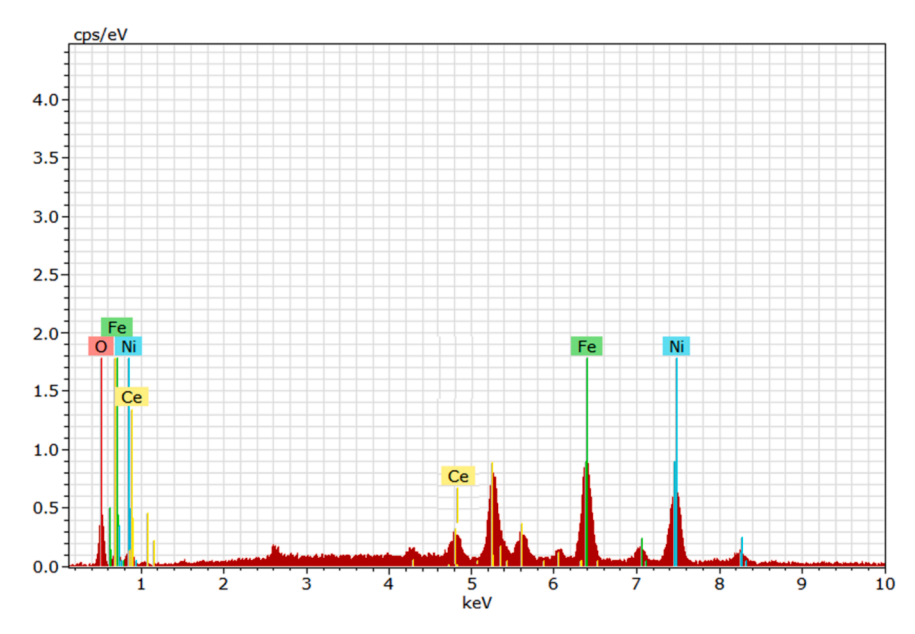
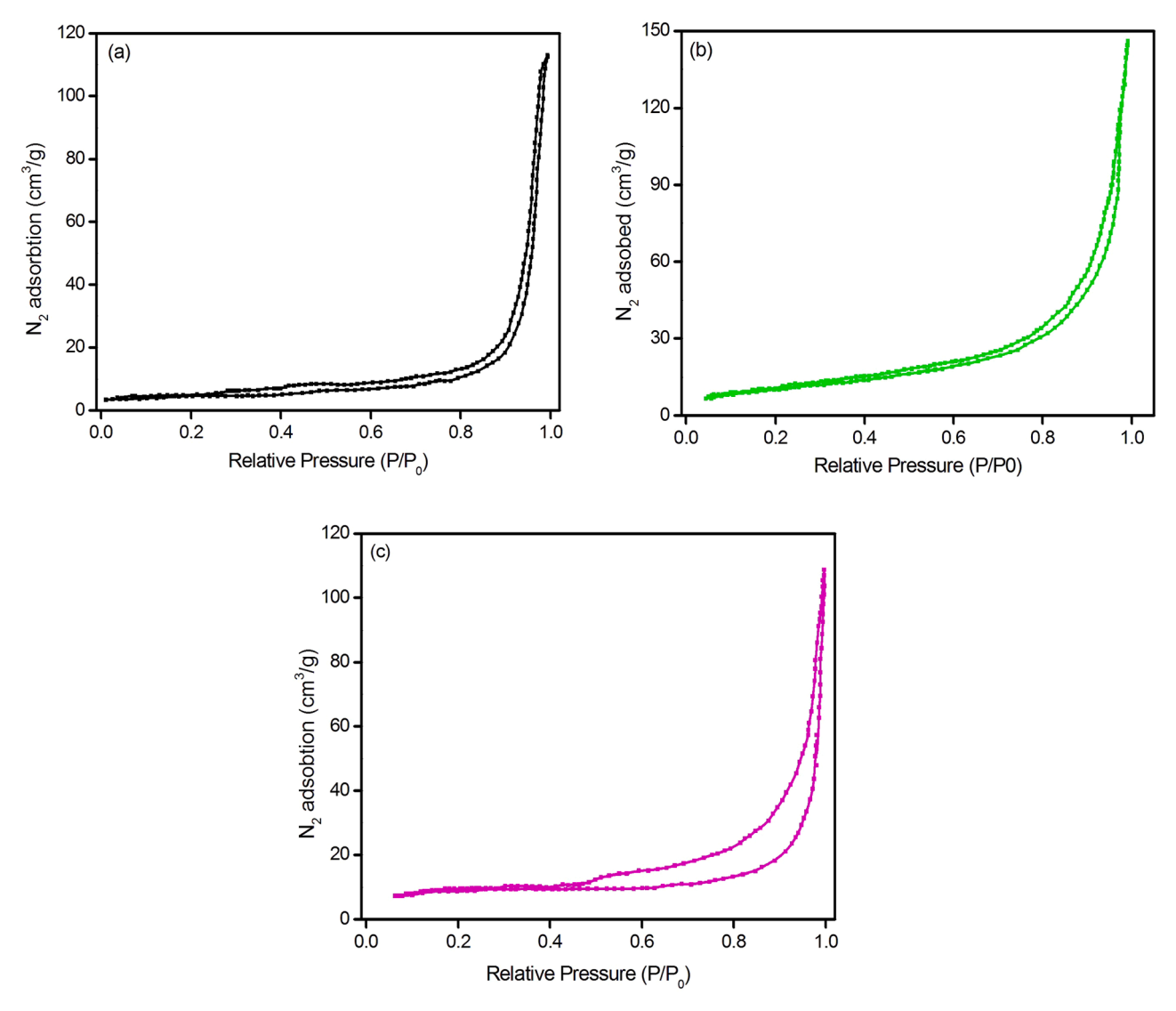


Fig. 15. EDS spectrum of NiCe $_{0.15}$ Fe  $_{1.85}$ O $_{4}$  sample.



 $\textbf{Fig. 16.} \ \ Adsorption \ is otherm \ of \ NiFe_{2}O_{4} \ (a), \ NiCe_{0.10}Fe_{1.90}O_{4} \ (b), \ and \ NiCe_{0.20}Fe_{1.80}O_{4} \ nanoparticles.$ 

poorly with adsorbant molecules considered, mainly, by adsorption heating lower than heating melt of the adsorbate.

Fig. 16(b&c) indicates the typical N<sub>2</sub> adsorption and desorption isotherm of NiCe<sub>0.10</sub>Fe<sub>1.90</sub>O<sub>4</sub> and NiCe<sub>0.20</sub>Fe<sub>1.80</sub>O<sub>4</sub> samples, respectively which indicates an increase in the amount of adsorbed N2 with the increase of the relative pressure, and adsorption follows a slightly different path to desorption and gives rise to a hysteresis loop. This kind of isotherm with H3 hysteresis loop is in general suggestive of the mesoporous porous nature of the material. Type IV isotherm with a hysteresis loop is related to capillary condensation occurring in the mesopores. Due to capillary condensation in pores during the adsorption and the changes in the pore's texture during the desorption process, the adsorption was high at higher pressure. The BET surface area was determined to be  $\sim$ 44.76 m<sup>2</sup>/g for nanocrystalline NiCe<sub>0.10</sub>Fe<sub>1.90</sub>O<sub>4</sub>,  $54.6 \text{ m}^2/\text{g}$  for NiCe<sub>0.20</sub>Fe<sub>1.80</sub>O<sub>4</sub>. The pore volume was determined to be  $0.1675 \text{ cm}^3/\text{g}$  for NiCe<sub>0.10</sub>Fe<sub>1.90</sub>O<sub>4</sub>, 0.0523 cm<sup>3</sup>/g for NiCe<sub>0.20</sub>Fe<sub>1.80</sub>O<sub>4</sub>. Likewise, the mean pore diameter of the NiCe<sub>0.10</sub>Fe<sub>1.90</sub>O<sub>4</sub> was 34.64 nm, and 15.20 nm for NiCe<sub>0.20</sub>Fe<sub>1.80</sub>O<sub>4</sub>. A decrease in crystallite size, followed by the formation of agglomerates, leads to an increase in the specific surface area. The greatest pore size distribution was observed from 5.0 to 47.6 nm and the small pore size distribution was in the range of 60.8 to 177.8 nm. Hence, it is confirmed that the NiCe<sub>0.10</sub>Fe<sub>1.0.1.90</sub>O<sub>4</sub> and NiCe<sub>0.20</sub>Fe<sub>1.80</sub>O<sub>4</sub> samples are composed almost of mesoporous. An increase in surface area would increase the active sites and make the redox reaction easy and make the ion transfer easier in the case of a supercapacitor. The result illustrates that the observed surface area and porous nature of the Ce-doped NiFe<sub>2</sub>O<sub>4</sub> may be useful in photocatalytic activity.

#### 3.8. VSM analysis

Fig. 17 illustrates the magnetization vs magnetic field curves of NiCe<sub>x</sub>Fe<sub>2-x</sub>O<sub>4</sub> nanoparticles (x = 0–0.20, in steps of 0.5). As the hysteresis is extremely low, and the curves are 's" shape, they indicate that all the samples are superparamagnetic. The values of coercivity ( $H_c$ ), saturation magnetization ( $M_s$ ), retentivity ( $M_r$ ), squareness ratio ( $M_r$ / $M_s$ ), magnetic anisotropy constant (K), and magnetic moment (K) were derived from the hysteresis loop and are presented in Table 8. The K10, K21 mu/g, and K22 mu/g, and 63.5 Oe, respectively. When the Ce content is increased to 0.15, K3 and K4 drop to 22.6 and 3.19 emu/g, respectively. Nonetheless, K5 rose to 130,9 Oe. K5 climbed to 25.8 emu/g, because of a further increase in K5, while K7 decreased to 2.40 emu/g and K6 decreased to

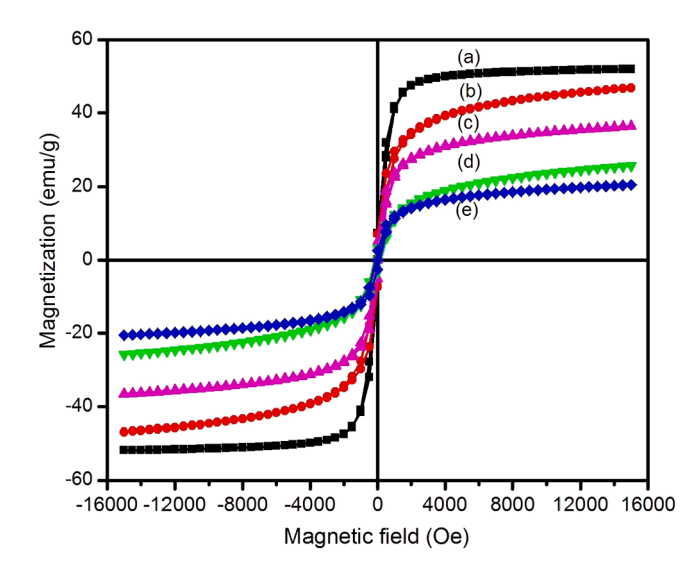


**Fig. 17.** Magnetic hysteresis (M-H) loops of the NiCe<sub>x</sub>Fe<sub>2-x</sub>O<sub>4</sub> nanoparticles. (a) x=0, (b) x=0.05, (c) x=0.10, (d) x=0.15 and (e) x=0.20.

Table 8 Coercivity  $(H_c)$ , remanent magnetization  $(M_r)$ , and saturation magnetization  $(M_s)$  of NiCe<sub>x</sub>Fe<sub>2-x</sub>O<sub>4</sub> nanoparticles obtained from VSM analysis.

Ce content 'x'	D <sub>W-H</sub> (nm)	H <sub>c</sub> (Oe)	M <sub>r</sub> (emu/ g)	M <sub>s</sub> (emu/ g)	$M_r/M_s$	$\begin{array}{c} \text{K (}\times\\ 10^3\text{ J/}\\ \text{m}^3\text{)} \end{array}$	$\eta_B$ (Bohr magneton)
0	53.3	63.5	7.27	51.9	0.140	6.163	2.4292
0.05	43.3	92.2	7.17	46.9	0.153	7.548	2.3384
0.10	40.8	118.6	5.05	36.5	0.139	6.559	2.5002
0.15	36.5	130.9	3.19	22.6	0.141	3.249	1.9658
0.20	42.0	50.2	2.40	25.8	0.093	3.306	1.7930

50.2 Oe. However, every sample remains superparamagnetic. The drop in magnetism (up to x=0.15) caused by the replacement of  ${\rm Fe}^{2+}$  ions can be explained as follows: When  ${\rm Ce}^{3+}$  ions are substituted into the NiFe<sub>2</sub>O<sub>4</sub> unit cell,  ${\rm Ce}^{3+}$  ions preferentially replace  ${\rm Fe}^{3+}$  ions at the B site, thereby decreasing the super-exchange interaction between the A and B sites.  ${\rm Fe}^{3+}$ - ${\rm Fe}^{3+}$  interactions are weakened as a result of the lessening in the content of  ${\rm Fe}^{3+}$  ions. In addition to the increased bond length produced by the enlargement of the unit cell, the super transfer field, superexchange, and double-exchange interactions were diminished [80]. A magnified version of M-H curves is displayed in Fig. 18.

In addition, the substitution of Ce<sup>3+</sup> ions with lesser magnetic moments for Fe<sup>3+</sup> ions reduces the magnetization of the resulting ferrite. Fig. 19 depicts the fluctuation of  $H_c$  and  $M_s$  versus  $Ce^{3+}$  concentration (x). The magnetic anisotropy and crystallite size of ferrite nanoparticles control their coercive field. The substitution of Fe<sup>3+</sup> ions with Ce<sup>3+</sup> ions increase the anisotropy of the crystal structure and, consequently, the magnetic field associated with it, increasing the coercive field H<sub>c</sub>. This continues up to x = 0.15 (solubility limit). Most available research articles indicate that  $H_c$  grows with crystallite size up to a certain threshold size (single domain size). After then, it declines [31]. However, our outcome is precisely the opposite of this. If we compare the coercive field  $H_c$  with the crystallite size given in Table 8, one can see that  $H_c$ increases with the reduction in crystallite size to 36.5 nm, and then there is a sudden decrease in  $H_c$  for the increase of crystallite size. This unusual property is shown in Fig. 20 that the  $H_c$  decreases hastily with crystallite size until the crystallite size of  $\sim$ 42 nm. After reaching a minimum  $H_c$  of 50.2 Oe at 41.8 nm, it increased to 92.2 Oe for the crystallite size of 43.3 nm and again decreased to 63.5 Oe for 53.3 nm. The reason for this unusual property may be the superparamagnetic property of all the samples. All are single-domain crystallites.

Each grain in magnetic materials comprises many domains, which

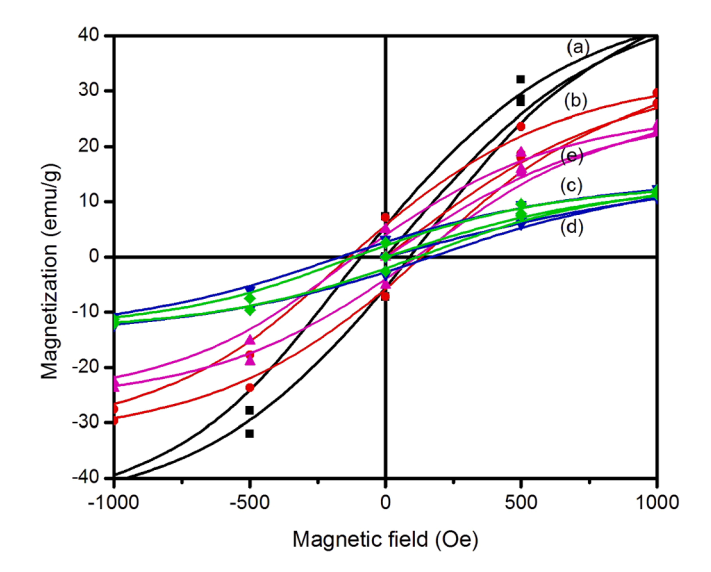


**Fig. 18.** Magnified version of M-H loops of the NiCe<sub>x</sub>Fe<sub>2-x</sub>O<sub>4</sub> nanoparticles; (a) x=0, (b) x=0.05, (c) x=0.10, (d) x=0.15 and (e) x=0.20.

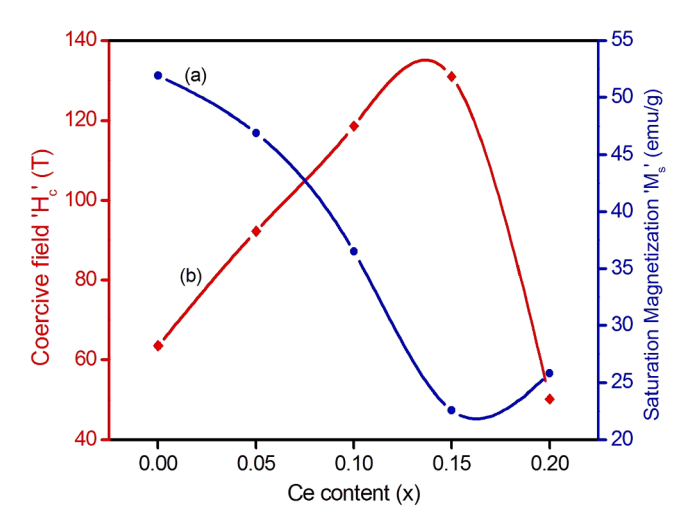
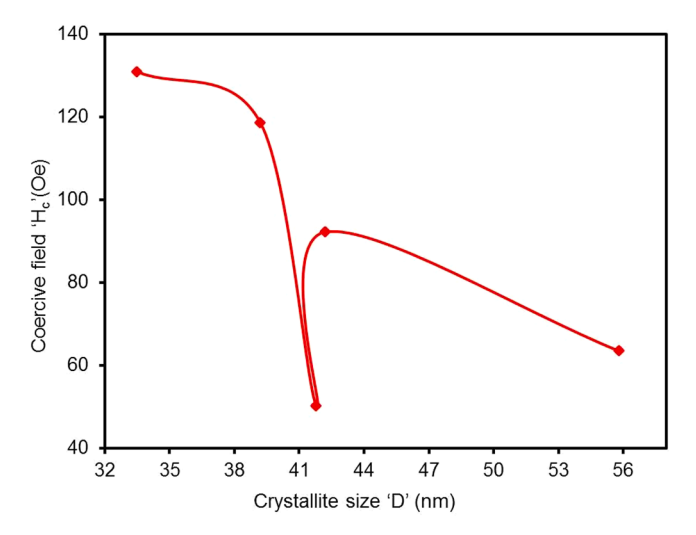


Fig. 19. Variation of (a) saturation magnetization  $M_{\text{s}}$  and (b) coercive field  $M_{\text{r}}$  with respect to Ce content (x).



**Fig. 20.** Relation between the crystallite size 'D' and coercive field ' $H_c$ ' shows that  $H_c$  decreases as the D increases till 41.8 nm, thereafter  $H_c$  increases with D.

are separated by barriers known as grain boundaries. As the Ce concentration rises, the grain size reduces, leading to an increase in the grain boundaries volume. Thus, the pinning effect of the domain wall at the grain boundary is intensified, making magnetization reversal more difficult and increasing coercivity. Therefore, a strong magnetic field is necessary for domain alignment. The grain borders serve as anchoring points. Consequently, the coercive field improves as particle size decreases. The increase in coercivity with decreasing crystallite size is accounted for the multi-domain nature of the samples. Interestingly, superparamagnetism has been observed in all the samples whose crystallite size varies from 55.8 to 33.5 nm. Therefore, our result confirms that the magnetization reversal properties appear to be independent of particle size. In the introduction part, it is mentioned that the superparamagnetic regime may exist in spherical NiFe<sub>2</sub>O<sub>4</sub> nanoparticles with sizes less than 15 nm. Also, we achieved superparamagnetism in NiFe<sub>2</sub>O<sub>4</sub> nanoparticles of size 53.3 nm, VSM analysis confirms that the single domain size in NiFe<sub>2</sub>O<sub>4</sub> nanoparticles may be around 56 nm.

From Table 8, it can be seen that  $H_c$  ranges from 63.5 Oe to 50.2 Oe, indicating a wide range of potential applications. The samples with  $H_c$  values between 60 and 100 Oe are utilized in longitudinal magnetic recording media, whilst  $H_c$  values greater than 120 Oe are utilized in transverse magnetic recording media [78]. The squareness ratio 'S'

quantifies the degree of squareness in the hysteresis loop and is mostly dependent on the microstructure. Remanence  $(M_r)$  is caused by the persistent rotation of domains and domain wall motion. In the case of polycrystalline materials, domain wall motion predominates over the more labor-intensive domain rotation. However, the nanostructural properties always impede domain wall motion, thereby influencing the shape of the loop. For magnetic fluids, 'S' should be very small or even nil, whereas for memory devices it should be sufficiently large. The measured squareness ratio of less than 0.5 confirmed the creation of randomly oriented single-domain nanoparticles with uniaxial anisotropy, which is a defining trait of the formation of domain walls and larger nanoparticles.

Fig. 21 illustrates how the sample squareness ratio and retentivity fluctuate with Ce content. The micro-strain of cerium-doped NiFe $_2$ O4 nanoparticles increases with dopant concentration, resulting in a decrease in  $M_r$ . The lower 'S' indicates that magnetic interactions between the particles are substantial. Due to the cubic anisotropic symmetry of magnetite, the M-H loop is controlled by the shape anisotropy of the square shape nanoparticles. K, the magnetic anisotropic constant, was computed using the formula presented here.

$$K = \frac{(M_s.H_c)}{0.64} \tag{24}$$

The calculation indicates that the value of K fell as the concentration of  $Ce^{3+}$  increased. This can be illustrated using the ratio of surface area to volume. When the particle size is decreased, the surface-to-volume ratio increases, resulting in a decrease in spin disorder on the surface of the nanoparticles and a corresponding decrease in the anisotropic constant K. The decrease in K values with increasing  $Ce^{3+}$  concentration validates ferromagnetism [81]. Using the formula, the magnetic moment per formula unit was empirically established, as given here

$$\mu_B = \frac{M_w \times M_s}{5584.86} \tag{25}$$

The magnetic parameters calculated from the M-H curves are displayed in Table 8. With an increase in  $Ce^{3+}$ ,  $\mu_B$  drops from 2.4292 to 1.7930, which shows the weakening of superexchange interactions in the case of  $Ce^{3+}$  doped NiFe<sub>2</sub>O<sub>4</sub> nanoparticles and is directly proportional to the saturation magnetization value.

The squareness ratios were calculated for all NiCe $_x$ Fe $_{2\cdot x}$ O $_4$  (x=0.00-0.20, insteps of 0.05) nanoparticles at room temperature. According to Stoner-Wohlfart's theory, the squareness ratios have a close value of 0.500 for uniaxial and 0.830 cubic anisotropy [82]. In this present work, squareness ratios have a range of 0.093–0.153 at room temperature, those are much lower than 0.500. These can be attributed

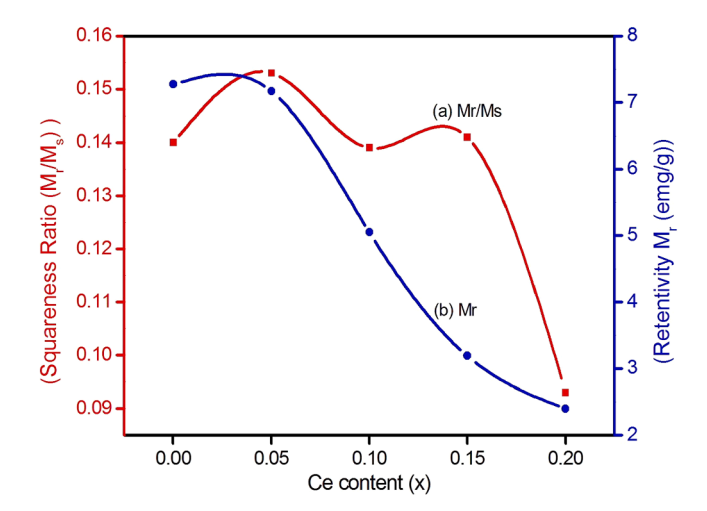


Fig. 21. Variation of (a) squareness ratio  $(M_s/M_r)$ , and (b) retentivity ' $M_r$ ' for various Ce content (x).

to surface spin disorder effects. It is considered that a magnetically disordered (or canted spin) shell region is present on the surface of the magnetic nanoparticles. For analysis purposes, the shape of the nanoparticles is considered as spherical. Then by using the values of  $M_s$  and D, the shell thickness (t) for the synthesized NiCe<sub>x</sub>Fe<sub>2-x</sub>O<sub>4</sub> (x = 0.00–0.20, insteps of 0.05) nanoparticles have been estimated. Supposing that the shell is magnetically "dead" (M = 0) and that "t" is independent of D<sub>XRD</sub>, the dependence of  $M_s$  on  $D_{XRD}$  is expressed [83] as

$$M_s^{(1/3)} = M_{(s,0)}^{(1/3)} \cdot \left[ 1 - \frac{2t}{D_{XRD}} \right]$$

Where  $M_{s,0}$  is the saturation magnetization for NiFe<sub>2</sub>O<sub>4</sub> at 0 K (52.93 emu/g). Since, we have approximate  $M_s$  values for NiCe<sub>x</sub>Fe<sub>2-x</sub>O<sub>4</sub> (x = 0.00-0.20, insteps of 0.05) nanoparticles at room temperature, then the corresponding shell average "t" was calculated to be 0.18 nm for NiFe<sub>2</sub>O<sub>4</sub>, 0.83 nm for NiCe<sub>0.05</sub>Fe<sub>1.95</sub>O<sub>4</sub>, 1.14 nm for NiCe<sub>0.10</sub>Fe<sub>1.90</sub>O<sub>4</sub>, 1.86 nm for NiCe<sub>0.15</sub>Fe<sub>1.85</sub>O<sub>4</sub>, and 2.28 nm for NiCe<sub>0.20</sub>Fe<sub>1.80</sub>O<sub>4</sub> and these values are in close agreement with the "t" value of 1.1 nm for NiFe<sub>2</sub>O<sub>4</sub> by mechano-synthesis [84]

#### 3.9. Electron paramagnetic resonance (EPR) spectra analysis

EPR spectroscopy relies heavily on the oxidation state, the local electronic structure, and the proximity of magnetic materials. Radiation interacts with the electronic spin, resulting in resonance. EPR spectroscopy can be used to analyze magnetic characteristics at higher frequencies. The magnetic anisotropy, as well as the size and shape of the magnetic nanoparticles, influence the intensity of the EPR signal. The location and area of the peak reveal the lattice's thermal motion and spin.

Fig. 22 depicts the EPR spectra of  $NiCe_xFe_{2-x}O_4$  (x=0–0.20, in steps of 0.05) nanoparticles recorded at 9.5 GHz (X-band) at ambient temperature. Using the formula provided here, the effective g-factor was computed.

$$g = \frac{h\nu}{\beta H_r} \tag{26}$$

Across the whole range of x, it can be observed that the spectra vary significantly. EPR signal is caused by magnetic interactions between magnetic ions Ni<sup>2+</sup> and Fe<sup>3+</sup>, specifically magnetic dipole interactions and super-exchange interactions. The narrow peak-to-peak line width  $(\Delta H_{\rm pp})$  indicates that super-exchange interactions are prominent, while

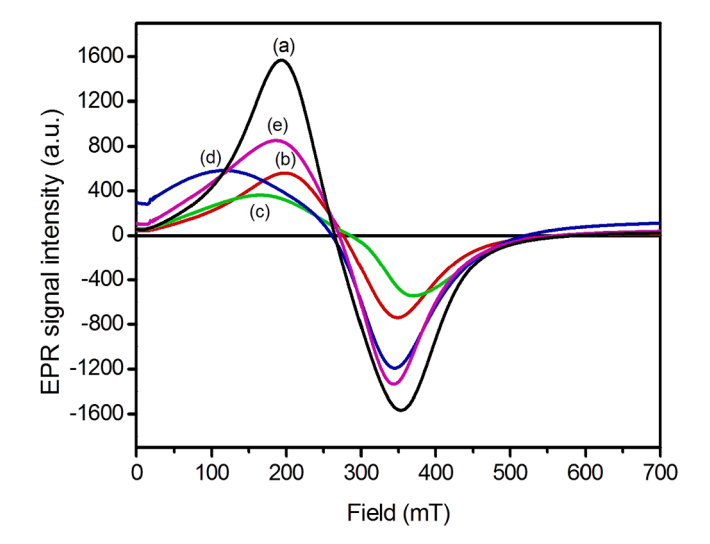


**Fig. 22.** EPR spectra of the NiCe<sub>x</sub>Fe<sub>2.x</sub>O<sub>4</sub> samples recorded at microwave frequency of 9.36 GHz: (a) x=0, (b) x=0.05, (c) x=0.10, (d) x=0.15 and (e) x=0.20.

the broad peak indicates that dipole interactions are dominating. Through anions, it can also be associated with the bond length between magnetic cations. The shorter bond lengths result in magnetic dipole interactions, whereas the longer bond lengths result in super-exchange interactions [85]. In our samples, the peak-to-peak linewidth increases from 117.60 mT to 234.30 mT as the Ce<sup>3+</sup> content grows from 0 to 0.15, which indicates the superexchange interactions of larger values of Ce ions, which is verified by the increased bond length. Additionally, it can be explained as follows: The techniques by which the spin magnetic moments relax back are distinct, including bulk rotation and Neel's rotation. If the nanoparticle's size is smaller than the critical diameter, then Neel's rotation occurs. The bulk rotation occurs like Neel's rotation in single-domain structures. TEM examination reveals that the particle size range of the NiFe<sub>2</sub>O<sub>4</sub> sample is 15-65 nm. The broadness of NiFe<sub>2</sub>O<sub>4</sub>'s EPR signal is caused by the bulk rotation of such particles. The magnetic moments of larger particles are shortened in the easy direction of magnetization, resulting in a shorter relaxation period and an increase in line width. The distance between these two peaks grows as x approaches 0.15, after which the spectral line becomes thinner and the peak-to-peak line width ( $\Delta H_{\rm pp})$  decreases. Consequently, the value of g was reduced from 2.59 (when x = 0) to 2.36 (when x = 0.10). The single resonance peak reveals the distribution of Fe<sup>3+</sup> in the octahedral site. Up to x = 0.10, the increase in the resonant magnetic field,  $H_r$ , indicates a drop in the internal magnetic field, which thereafter begins to diminish. The drop in the g-value as the concentration of  $Ce^{3+}$  increases from x =0.10 to 0.10 suggests that the magnetic moment has intensified and that the superexchange interaction between cations with the assistance of oxygen ions has strengthened. Due to the anisotropic arrangement of magnetic moments, the value of g decreases till x = 0.10 [86]. The greater ionic radii of Ce<sup>3+</sup> ions in comparison to Fe<sup>3+</sup> have been reported to cause lattice expansion in ferrites, which can modify the superexchange interaction of Fe<sup>3+</sup>-O<sup>2-</sup>-Fe<sup>3+</sup>. The spin-spin relaxation time constant  $(\tau)$  was computed using the relationship presented here.

$$\tau = \frac{\hbar}{g\beta\Delta H_{1/2}} \tag{27}$$

where  $\hbar=1.054\times 10^{\cdot 27}$  is a constant,  $\beta$  is the Bohr Magneton (9.27  $\times$   $10^{-24}$  J/T),  $\Delta H_{1/2}$  is the linewidth at half height of the absorption peak and is given by,

$$\Delta H_{1/2} = \sqrt{3} \Delta H_{PP} \tag{28}$$

Magnetic parameters such as g-value, resonant magnetic field  $(H_r)$ , peak-to-peak line width  $(\Delta H_{PP})$ , and spin-spin relaxation time constant  $(\tau)$  were computed and listed in Table 9.

# 4. Conclusions

In summary,  ${
m NiCe}_x{
m Fe}_{2.x}{
m O}_4$  (x=0–0.20, in steps of 0.5) nanoparticles were effectively prepared by chemical precipitation method. The x-ray diffraction study exposed that the synthesized samples are single-phase and possess cubic structures. The XRD analysis also confirmed the reduction in average crystallite size from 55.8 nm to 33.5 nm as Ce content climbed from 0 to 0.15, and then increased to 41.8 nm when x

**Table 9** Resonance field  $(H_r)$ , g value, and  $\Delta H_{pp}$  of NiCe<sub>x</sub>Fe<sub>2-x</sub>O<sub>4</sub> nanoparticles obtained from EPR analysis.

Ce content 'x'	$H_r$ ( $\times$ $10^{-3}$ T)	g value	Ipp	$\Delta H_{pp}$ ( $\times$ $10^{-3}$ T)	ΔH <sub>1/2</sub> (T)	T ( × 10 <sup>-11</sup> s)
0	260.85	2.59	3045.33	117.60	203.69	2.158
0.05	276.76	2.44	1300.62	150.13	260.03	1.794
0.10	286.29	2.36	905.14	211.70	366.68	1.317
0.15	271.81	2.57	1774.22	234.30	405.82	1.091
0.20	268.93	2.51	2052.51	160.43	277.87	1.631

reached 0.20. UV-visible-NIR spectroscopy revealed that by raising the  $Ce^{3+}$  ions from 0 to 0.15, the  $E_g$  of NiFe<sub>2</sub>O<sub>4</sub> may be extended from 1.5 to 1.95 eV. The two absorption bands at around 603 and 420 cm<sup>-1</sup> confirmed the presence of tetrahedral and octahedral sites, respectively in the ferrite nanoparticles, as determined by FTIR. The fact that ceriumdoped nickel ferrites emit red light (705 nm) indicates that they are appropriate for use in optoelectronic devices. The TEM investigation finds that NiFe<sub>2</sub>O<sub>4</sub> square shape particles are sensitive to Ce doping and favor microstructural change from a square shape to elongated spherical shape nanoparticles, confirming once again that many nanostructures can be generated using a simple co-precipitation technique. The BET result illustrates that Ce doping creates pores in nickel ferrite therefore Ce-doped NiFe<sub>2</sub>O<sub>4</sub> may be useful in photocatalytic activity. The M<sub>s</sub>, M<sub>r</sub>, and H<sub>c</sub> all reduced with increasing Ce content to a minimum of 22.6 emu/g, 2.4 emu/g, and 50.2 Oe for x = 0.20 in NiCe<sub>x</sub>Fe<sub>2-x</sub>O<sub>4</sub> nanoparticles, and all samples displayed significant superparamagnetic behavior with limited hysteresis loss. VSM analysis also concludes that the single domain size in NiFe<sub>2</sub>O<sub>4</sub> nanoparticles may be around 56 nm. The electron paramagnetic resonance investigation shows that a higher Ce content surges the superexchange interaction, which is diminished at lower Ce concentrations. Thus, the current analysis accomplishes that cerium can be substituted with NiFe<sub>2</sub>O<sub>4</sub> up to x = 0.20 short of the formation of secondary phases through a simple co-precipitation method (Fig. 8).

### **Funding statement**

Authors did not receive any financial support neither from their institution nor from funding agencies

#### Data availability

The authors confirm that the data supporting the findings of this research are available with the corresponding author on reasonable request.

#### CRediT authorship contribution statement

**P. Priyadharshini:** Data curation, Formal analysis, Investigation, Conceptualization, Methodology, Writing – original draft. **K. Pushpanathan:** Conceptualization, Methodology, Supervision, Validation, Project administration, Writing – review & editing.

# **Declaration of Competing Interest**

The authors declare that they have no known competing financial interests or personal relationships that could have appeared to influence the work reported in this research article.

# Data availability

Data will be made available on request.

#### Acknowledgments

The authors are grateful to SAIF (IIT – Madras) - Chennai for providing VSM and EPR characterizations, and STIC – Cochin for providing TEM facilities.

#### References

[1] Y. Slimani, B. Unal, M.A. Almessiere, E. Hannachi, G. Yasin, A. Baykal, I. Ercan, Role of WO<sub>3</sub> nanoparticles in electrical and dielectric properties of BaTiO<sub>3</sub>-SrTiO<sub>3</sub> ceramics, J. Mater. Sci.: Mater. Electron. 31 (2020) 7786–7797, https://doi.org/ 10.1007/s10854-020-03317-7.

- [2] Y. Slimani, E. Hannachi, M.K. Ben Salem, A. Hamrita, M.B. Salem, F. Ben Azzouz, Excess conductivity study in nano-CoFe<sub>2</sub>O<sub>4</sub>-added YBa<sub>2</sub>Cu<sub>3</sub>O<sub>7-d</sub> and Y<sub>3</sub>Ba<sub>5</sub>Cu<sub>8</sub>O<sub>18</sub>  $_{\pm x}$  superconductors, J. Supercond. Nov. Magn. 28 (2015) 3001–3010, https://doi.org/10.1007/s10948-015-3144-0.
- [3] Y. Slimani, M.A. Almessiere, M. Nawaz, A. Baykal, S. Akhtar, I. Ercan, I. Belenli, Effect of bimetallic (Ca, Mg) substitution on magneto-optical properties of Fe<sub>2</sub>O<sub>4</sub> nanoparticles, Ceram. Int. 45 (2019) 6021–6029, https://doi.org/10.1016/j. ceramint 2018 12 022
- [4] M.A. Almessiere, Y. Slimani, S. Rehman, F.A. Khan, Ç.D. Gunguneş, S. Guner, S. E. Shirsath, A. Baykal, Magnetic properties, anticancer and antibacterial effectiveness of sonochemically produced Ce<sup>3+</sup>/Dy<sup>3+</sup> co-activated Mn-Zn nanospinel ferrites, Arab. J. Chem. 13 (2020) 7403–7417, https://doi.org/10.1016/j.arabjc.2020.08.017.
- [5] M.A.A. S.Rehman, A.B. N.Tashkandi, Y. Slimani, R. Jermy, C.Y. R.Vijaya, Fabrication of spinel cobalt ferrite (CoFe<sub>2</sub>O<sub>4</sub>) nanoparticles with unique earth element cerium and neodymium for anticandidal activities, Chem. Select 4 (2019) 14329–14334, https://doi.org/10.1002/slct.201901811.
- [6] M.H.A. Mhareb, Y. Slimani, Y.S. Alajerami, M.I. Sayyed, Eloic Lacomme, M. A. Almessiere, Structural and radiation shielding properties of BaTiO<sub>3</sub> ceramic with different concentrations of Bismuth and Ytterbium, Ceram. Int. 46 (2020) 28877–28886, https://doi.org/10.1016/j.ceramint.2020.08.055.
- [7] Y. Slimani, B. Unal, E. Hannachi, A. Selmi, M.A. Almessiere, M. Nawaz, A. Baykal, I. Ercan, M. Yildiz, Frequency and dc bias voltage dependent dielectric properties and electrical conductivity of BaTiO<sub>3</sub> single bond SrTiO<sub>3</sub>/(SiO<sub>2</sub>)<sub>x</sub> nanocomposites, Ceram. Int. 45 (2019) 11989–12000, https://doi.org/10.1016/j.ceramint.2019.03.092.
- [8] Y. Slimani, A. Selmi, E. Hannachi, M.A. Almessiere, M. Mumtaz, A. Baykal, I. Ercan, Study of tungsten oxide effect on the performance of BaTiO<sub>3</sub> ceramics, J. Mater. Sci.: Mater. Electron. 30 (2019) 13509–13518, https://doi.org/10.1007/s10854-019-01718-x.
- [9] M.K. Ben Salem, E. Hannachi, Y. Slimani, A. Hamrita, M. Zouaoui, L. Bessais, M. Ben Salem, F. Ben Azzouz, SiO<sub>2</sub> nanoparticles addition effect on microstructure and pinning properties in YBa<sub>2</sub>Cu<sub>3</sub>O<sub>y</sub>, Ceram. Int. 40 (2014) 4953–4962, https://doi.org/10.1016/j.ceramint.2013.10.103.
- [10] A. Hamrita, Y. Slimani, M.K. Ben Salem, E. Hannachi, L. Bessais, F. Ben Azzouz, M. B. Salem, Superconducting properties of polycrystalline YBa<sub>2</sub>Cu<sub>3</sub>O<sub>7-d</sub> prepared by sintering of ball-milled precursor powder, Ceram. Int. 40 (2014) 1461–1470, https://doi.org/10.1016/j.ceramint.2013.07.030.
- [11] E. Hannachi, M.A. Almessiere, Y. Slimani, A. Baykal, F. Ben Azzouz, AC susceptibility investigation of YBCO superconductor added by carbon nanotubes, J. Alloys Compd. 812 (2020), 152150, https://doi.org/10.1016/j.iallcom.2019.152150.
- [12] M.A. Ansari, H.M. Albetran, M.H. Alheshibri, A. Timoumi, N.A. Algarou, S. Akhtar, Y. Slimani, M.A. Almessiere, F.S. Alahmari, A. Baykal, I.M. Low, Synthesis of electrospun TiO2 nanofibers and characterization of their antibacterial and antibiofilm potential against gram-positive and gram-negative bacteria, Antibiotics 9 (2020) 572, https://doi.org/10.3390/antibiotics9090572.
- [13] Y. Slimani, M.A. Almessiere, E. Hannachi, M. Mumtaz, A. Manikandan, A. Baykal, F. Ben Azzouz, Improvement of flux pinning ability by tungsten oxide nanoparticles added in YBa<sub>2</sub>Cu<sub>3</sub>O<sub>y</sub> superconductor, Ceram. Int. 45 (2019) 6828–6835, https://doi.org/10.1016/j.ceramint.2018.12.176.
- [14] E. Hannachi, Y. Slimani, M. Nawaz, Z. Trabelsi, G. Yasin, M. Bilal, M.A. Almessiere, A. Baykal, A. Thakur, P. Thakur, Synthesis, characterization, and evaluation of the photocatalytic properties of zinc oxide co-doped with lanthanides elements, J. Phys. Chem. Solids 170 (2022) 11091, https://doi.org/10.1016/j. jpcs.2022.110910.
- [15] E. Hannachi, Y. Slimani, M. Nawaz, R. Sivakumar, Z. Trabelsi, R. Vignesh, S. Akhtar, M.A. Almessiere, A. Baykal, G. Yasin, Preparation of cerium and yttrium doped ZnO nanoparticles and tracking their structural, optical, and photocatalytic performances, J. Rare Earths (2022), https://doi.org/10.1016/j.jre.2022.03.020.
- [16] Y. Slimani, E. Hannachi, A. Ekicibil, M.A. Almessiere, F. Ben Azzouz, Investigation of the impact of nano-sized wires and particles TiO2 on Y-123 superconductor performance, J. Alloys Compd. 43 (2019) 664–673, https://doi.org/10.1016/j. iallcom. 2018.12.062
- [17] Superconducting Materials: fundamentals, Synthesis and Applications Editors: Y. Slimani, E. Hannachi. doi:10.1007/978-981-19-1211-5.
- [18] S. Laurent, S. Boutry, R.N. Muller, Metal oxide particles and their prospects for applications. Chapter 1, Page No 7. doi:10.1016/B978-0-08-101925-2.00001-2.
- [19] M. Manikandan, K. Yogasundari, A. Thanrasu, K. Dinesh, K. Kanmani Raja, Y. Slimani, S.K. Jaganathan, R. Srinivasan, A. Baykal, Structural, morphological and optical properties of multifunctional magnetic-luminescent ZnO@Fe<sub>3</sub>O<sub>4</sub> nanocomposite, Phys. E: Low-Dimens. Syst. Nanostruct. 124 (2020), 114291, https://doi.org/10.1016/j.physe.2020.114291.
- [20] G. Yasin, M.J. Anjum, M.U. Malik, M.A. Khan, W.Q. Khan, M. Arif, T. Mehtab, T. A. Nguyen, Y. Slimani, M. Tabish, Y.Z. D.Ali, Revealing the erosion-corrosion performance of sphere-shaped morphology of nickel matrix nanocomposite strengthened with reduced graphene oxide nanoplatelets, Diam. Relat Mater. 104 (2020), 107763, https://doi.org/10.1016/j.diamond.2020.107763.
- [21] P.N. Dave, R. Sirach, Catalytic performance of nano-sized cobalt copper ferrite on thermal decomposition of ammonium nitrate, Chem. Phys. Impact 6 (2023), 100155, https://doi.org/10.1016/j.chphi.2022.100155.
- [22] M.A. Almessiere, Y. Slimani, M. Sertkol, M. Nawaz, A. Baykal, I. Ercan, The impact of Zr substituted Sr hexaferrite: investigation on structure, optic and magnetic properties, Results Phys. 13 (2019), 102244, https://doi.org/10.1016/j. rinp.2019.102244.

- [23] M.A. Almessiere, Y. Slimani, H.S. El Sayed, A. Baykal, Morphology and magnetic traits of strontium nanohexaferrites: effects of manganese/yttrium co-substitution, J. Rare Earths 37 (2019) 732–740, https://doi.org/10.1016/j.jre.2018.09.014.
- [24] M.A. Almessiere, Y. Slimani, H.S. El Sayed, A. Baykal, I. Ercan, Microstructural and magnetic investigation of vanadium-substituted Sr-nano hexaferrite, J. Magn. Magn. Mater. 471 (2019) 124–132, https://doi.org/10.1016/j. immp. 2018.09.054
- [25] M.A. Almessiere, Y. Slimani, H.S. El Sayed, A. Baykal, Structural and magnetic properties of Ce-Y substituted strontium nanohexaferrites, Ceram. Int. 44 (2018) 12511–12519, https://doi.org/10.1016/j.ceramint.2018.04.045.
- [26] M.A. Almessiere, Y. Slimani, A.V. Trukhanov, A. Baykal, H. Gungunes, E. L. Trukhanova, S.V. Trukhanov, V.G. Kostishin, Strong correlation between Dy<sup>3+</sup> concentration, structure, magnetic and microwave properties of the [Ni<sub>0.5</sub>Co<sub>0.5</sub>] (Dy<sub>x</sub>Fe<sub>2-x</sub>)O<sub>4</sub> nanosized ferrites, J. Ind. Eng. Chem. 90 (2020) 251–259, https://doi.org/10.1016/j.ijec.2020.07.020.
- [27] B. Ita, P. Murugavel, V. Ponnambalam, A.R. Raju, Magnetic properties of lanthanum orthoferrite fine powders prepared by different chemical routes, J. Chem. Sci. 115 (2003) 519–524, https://doi.org/10.1007/BF02708243.
- [28] A. Chaudhari, T. Kaida, H.B. Desai, S. Ghosh, R.P. Bhatt, A.R. Tanna, Dye degradation and antimicrobial applications of manganese ferrite nanoparticles synthesized by plant extracts, Chem. Phys. Impact 5 (2022), 100098, https://doi. org/10.1016/j.chphi.2022.100098.
- [29] R. Tiwari, M. De, H.S. Tewari, S.K. Ghoshal, Structural and magnetic properties of tailored NiFe<sub>2</sub>O<sub>4</sub> nanostructures synthesized using auto-combustion method, Results Phys. 16 (2020), 102916, https://doi.org/10.1016/j.rinp.2019.102916.
- [30] A. Juliet Christina Mary, C.I. Sathish, P.S.M. Kumar, A. Vinu, A. Chandra Bose, Fabrication of hybrid supercapacitor device based on NiCo<sub>2</sub>O<sub>4</sub>@ZnCo<sub>2</sub>O<sub>4</sub> and the biomass-derived N-doped activated a carbon with honeycomb structure, Electrochim. Acta 342 (2020), 136062, https://doi.org/10.1016/j. electacta.2020.136062.
- [31] S. Joshi, M. Kumar, S. Chhoker, G. Srivastava, M. Jewariya, V.N. Singh, Structural, magnetic, dielectric, and optical properties of nickel ferrite nanoparticles synthesized by co-precipitation method, J Mol. Struct. 1076 (2014) 55–62, https://doi.org/10.1016/j.molstruc.2014.07.048.
- [32] G. Vinothkumar, S. Rengaraj, P. Arunkumar, S.W. Cha, K. Suresh Babu, Ionic radii and concentration dependency of RE<sup>3+</sup> (Eu<sup>3+</sup>, Nd<sub>3+</sub>, Pr<sup>3+</sup>, and La<sup>3+</sup>)doped cerium oxide nanoparticles for enhanced multienzyme-mimetic and hydroxyl radical scavenging activity, J. Phys. Chem. C 123 (2019) 541–553, https://doi.org/10.1021/acs.jpcc.8b10108.
- [33] M.N. Akhtar, A.B. Sulong, M.N. Akhtar, M.A. Khan, Systematic study of Ce<sup>3+</sup> on the structural and magnetic properties of Cu nanosized ferrites for potential applications, J. Rare Earths 36 (2018) 156–164, https://doi.org/10.1016/j. ire.2017.09.003.
- [34] T. Roman, A. Pui, A.V. Lukacs, N. Cimpoesu, A.I.B. S.Lupescu, K. Kordatos, A. Ntziouni, P. Postolache, M. Zaharia, S. Stanciu, L. Mitoşeriu, Structural changes of cerium doped copper ferrites during sintering process and magneto-electrical properties assessment, Ceram. Int. 45 (2019) 17243–17251, https://doi.org/ 10.1016/j.ceramint.2019.05.280.
- [35] M.A. Almessiere, Y. Slimani, S. Güner, A. Baykal, I. Ercan, Effect of dysprosium substitution on magnetic and structural properties of NiFe<sub>2</sub>O<sub>4</sub> nanoparticles, J. Rare Earths 37 (2019) 871–878, https://doi.org/10.1016/j.jre.2018.10.009.
- [36] M.A. Almessiere, Y. Slimani, H. Gungunes, S. Ali, A. Manikandan, I. Ercan, A. Baykal, A.V. Trukhanov, Magnetic attributes of NiFe<sub>2</sub>O<sub>4</sub> nanoparticles: influence of dysprosium ions (Dy<sup>3+</sup>) substitution, Nanomaterials 9 (2019) 820, https://doi. org/10.3390/2Fnano9060820.
- [37] M.A. Almessiere, Y. Slimani, M. Sertkol, M. Nawaz, A. Sadaqat, A. Baykal, I. Ercan, B. Ozçelik, Effect of Nb<sup>3+</sup> substitution on the structural, magnetic, and optical properties of Co<sub>0.5</sub>Ni<sub>0.5</sub>Fe<sub>2</sub>O<sub>4</sub> nanoparticles, Nanomaterials 9 (2019) 430, https://doi.org/10.3390/2Fnano9030430.
- [38] M.A. Almessiere, Y. Slimani, H. Gungunes, V.G. Kostishyn, S.V. Trukhanov, A. V. Trukhanov, A. Baykal, Impact of Eu<sup>3+</sup> ion substitution on structural, magnetic and microwave traits of Ni–Cu–Zn spinel ferrites, Ceram. Int. 46 (2020) 11124–11131, https://doi.org/10.1016/j.ceramint.2020.01.132.
- [39] B. Unal, M.A. Almessiere, A. Baykal, Y. Slimani, A. Sadaqat, Anwar Ul-Hamid, A study on the electrical and dielectric traits of ternary NiCuZn-spinel ferrites co-substituted with Ga<sup>3+</sup>-Gd<sup>3+</sup> ions, Mater. Sci. Eng. B 289 (2023), 116249, https://doi.org/10.1016/j.mseb.2022.116249.
- [40] M.A. Almessiere, B. Unal, Y. Slimani, A.D. Korkmaz, A. Baykal, I. Ercan, Electrical properties of La<sup>3+</sup> and Y<sup>3+</sup> ions substituted Ni<sub>0.3</sub>Cu<sub>0.3</sub>Zn<sub>0.4</sub>Fe<sub>2</sub>O<sub>4</sub> nanospinel ferrites, Results Phys. 15 (2019), 102755, https://doi.org/10.1016/j.rinp.2019.102755.
- [41] G. Nabi, W. Raza, M.A. Kamran, T. Alharbi, M. Rafique, M.B. Tahir, S. Hussain, N. R. Khalid, Q. ul-Aain, N. Malik, R.S. Ahmed, C.B. Cao, Role of cerium-doping in CoFe<sub>2</sub>O<sub>4</sub> electrodes for high performance supercapacitors, J. Energy Storage 29 (2020), 101452, https://doi.org/10.1016/j.est.2020.101452.
- [42] G. Dixit, J.P. Singh, R.C. Srivastava, H.M. Agarwal, Structural, optical and magnetic studies of Ce doped NiFe<sub>2</sub>O<sub>4</sub> nanoparticles, J. Magn. Magn. Mater. 345 (2013) 65–71, https://doi.org/10.1016/j.jmmm.2013.05.060.
- [43] K. Elayakumar, V. Sathana, R.T. Kumar, Structural and magnetic characterization of rare-earth element cerium-doped nickel ferrite nanoparticles (NiCe<sub>x</sub>Fe<sub>2-x</sub>O<sub>4</sub>) by sol-gel method with anti-bacterial activity, J. Supercond. Nov. Magn. 33 (2020) 2171–2178, https://doi.org/10.1007/s10948-020-05475-5.
- [44] G. Dixit, P. Negi, J.P. Singh, R.C. Srivastava, H.M. Agrawal, Effect of Ce doping on the magnetic properties of NiFe<sub>2</sub>O<sub>4</sub> nanoparticles, J. Supercond. Nov. Magn. 26 (2013) 1015–1019, https://doi.org/10.1007/s10948-012-1847-z.

- [45] M. Maheen, K. Rafeekali, R. Sebastian, E.M. Mohammed, Structural and dielectric studies of cerium substituted nickel ferrite nanoparticle, Int. J. Eng. Sci. 4 (2015) 33–37. https://www.theijes.com/papers/v4-i5/Version-3/F0453033037.pdf.
- [46] G. Dixit, J.P. Singh, R.C. Srivastava, H.M. Agrawal, Magnetic resonance study of Ce and Gd doped NiFe<sub>2</sub>O<sub>4</sub> nanoparticles, J. Magn. Magn. Mater. 324 (2012) 479–483, https://doi.org/10.1016/j.jmmm.2011.08.027.
- [47] M.M.L. Sonia, S. Anand, V.M. Vinosel, M.A. Janifer, S. Pauline, Effect of lattice strain on structural magnetic and dielectric properties of sol-gel synthesized nanocrystalline Ce<sup>3+</sup> substituted nickel ferrite, J Mater Sci: Mater. Electron. 29 (2018) 15006–15021, https://doi.org/10.1007/s10854-018-9639-2.
- [48] K. Elayakumar, A. Manikandan, A. Dinesh, K. Thanrasu, K. Kanmani Raja, R. Thilak Kumar, Y. Slimani, S.K. Jaganathan, A. Baykal, Enhanced magnetic property and antibacterial biomedical activity of Ce<sup>3+</sup> doped CuFe<sub>2</sub>O<sub>4</sub> spinel nanoparticles synthesized by sol-gel method, J. Magn. Magn. Mater. 478 (2019) 140–147, https://doi.org/10.1016/j.jmmm.2019.01.108.
- [49] M.A. Almessiere, B. Unal, Y. Slimani, H. Gungunes, M.S. Toprak, N. Tashkandi, A. Baykal, M. Sertkol, A.V. Trukhanov, A. Yıldız, A. Manikandan, Effects of Ce–Dy rare earths co-doping on various features of Ni–Co spinel ferrite microspheres prepared via hydrothermal approach, J. Mater. Res. Technol. 14 (2021) 2534–2553, https://doi.org/10.1016/j.jmrt.2021.07.142.
- [50] Y. Slimani, B. Unal, M.A. Almessiere, A. Demir Korkmaz, S.E. Shirsath, G. Yasin, A. V. Trukhanov, A. Baykal, Investigation of structural and physical properties of Eu<sup>3</sup> <sup>+</sup> ions substituted Ni<sub>0,4</sub>Cu<sub>0,2</sub>Zn<sub>0,4</sub>Fe<sub>2</sub>O<sub>4</sub> spinel ferrite nanoparticles prepared via sonochemical approach, Results Phys. 17 (2020), 103061, https://doi.org/10.1016/j.rinp.2020.103061
- [51] S.A. Al-Zahrani, A. Manikandan, K. Thanrasu, A. Dinesh, K. Kanmani Raja, M. A. Almessiere, Y. Slimani, A. Baykal, S. Bhuminathan, S. Raghavendra Jayesh, J. Ahmed, H.S. Alorfi, M.A. Hussein, I. Khan, A. Khan, Influence of Ce<sup>3+</sup> on the structural, morphological, magnetic, photocatalytic and antibacterial properties of spinel MnFe<sub>2</sub>O<sub>4</sub> nanocrystallites prepared by the combustion route, Crystals 12 (2022) 268, https://doi.org/10.3390/cryst12020268.
- [52] J.P. Singh, G. Dixit, R.C. Srivastava, H.M. Agrawal, K. Asokan, Looking for possibility of multiferroism in NiGd<sub>0.04</sub>Fe<sub>1.96</sub>O<sub>4</sub> nanoparticle system, J. Phys. D: Appl. Phys. 44 (2011), 435306, https://doi.org/10.1088/0022-3727/44/43/ 435306.
- [53] D. Guragain, R.B. Rai, S. Yoon, T.P. Poudel, S.C. Bhandari, S.R. Mishra, Effect of terbium ion substitution in inverse spinel nickel ferrite: structural and magnetic study, Magnetochemistry 6 (2020) 14, https://doi.org/10.3390/ magnetochemistry6010014.
- [54] P. Scherrer, Gottinger Nachritchten Gesell Bestimung der innerenstruktw und der grobe von kolloidteilchenmittels, Rontgenstrahlen 2 (1918) 98. http://eudml.org/ doc/59018.
- [55] L. Zhao, H. Yang, X. Zhao, L. Yu, Y. Cui, S. Feng, Magnetic properties of CoFe<sub>2</sub>O<sub>4</sub> ferrite doped with rare earth ion, Mater. Lett. 60 (2006) 1–6, https://doi.org/10.1016/j.matlet.2005.07.017.
- [56] S. Manouchehri, Z. Ghasemian, D. Shahbazi-Gahrouei, M. Abdolahi, Synthesis and characterization of cobalt-zinc ferrite nanoparticles coated with DMSA, Chem. Express 2 (2013) 147–152.
- [57] P. Priyadharshini, K. Pushpanathan, Tuning of crystallite size, energy gap and magnetic property of Mn doped CoFe<sub>2</sub>O<sub>4</sub> nanoparticles, Surf. Rev. Lett. 8 (2021), 2150052, https://doi.org/10.1142/S0218625X21500529.
- [58] G.K. Williamson, W.H. Hall, X-ray line broadening from filed aluminium and wolfram, Acta Metall. 1 (1953) 22–31, https://doi.org/10.1016/0001-6160(53) 90006-6
- [59] E.S. Bakeer, A.I. Abou-Aly, N.H. Mohammed, R. Awad, M. Hasebbo, Characterization and magnetic properties of nanoferrite ZnFe<sub>2-x</sub>La<sub>x</sub>O<sub>4</sub> prepared by co-precipitation method, J. Supercond. Nov. Magn. 30 (2017) 893–902, https:// doi.org/10.1007/s10948-016-3876-5.
- [60] P. Monisha, P. Priyadharshini, S.S. Gomathi, K. Pushpanathan, Influence of Mn dopant on the crystallite size, optical and magnetic behaviour of CoFe<sub>2</sub>O<sub>4</sub> magnetic nanoparticles, J. Phys. Chem. Solids 148 (2021), 109654, https://doi.org/ 10.1016/i.jpcs.2020.109654.
- [61] H.K. Dubey, P. Lahiri, Synthesis, structural, dielectric and magnetic properties of Cd based Mn nanosized ferrites, Mater. Technol. 36 (2020) 131–144, https://doi. org/10.1080/10667857.2020.1734728.
- [62] Z.H. Yamani, Magnetic properties and photocatalytic degradation performance of MFe<sub>2</sub>O<sub>4</sub> (M=Co,Ni)/BiOCl composites catalysts under UV light irradiation, Arab. J. Sci. Eng. 43 (2018) 383–388, https://doi.org/10.1007/s13369-017-2623-y.
- [63] M.G. Naseri, M.H.M. Ara, E.B. Saion, A.H. Shaari, Superparamagnetic magnesium ferrite nanoparticles fabricated by a simple, thermal-treatment method, J. Magn. Magn. Mater. 350 (2014) 141–147, https://doi.org/10.1016/j. immm 2013.08.032
- [64] S.R. Patade, D.D. Andhare, P.B. Kharat, A.V. Humbe, K.M. Jadhav, Impact of crystallites on enhancement of bandgap of Mn<sub>1-x</sub>Zn<sub>x</sub>Fe<sub>2</sub>O<sub>4</sub> (1≥x≥0) nanospinels, Chem. Phys. Lett. 745 (2020), 137240, https://doi.org/10.1016/j.cplett.2020.137240
- [65] A.D. Korkmaz, S. Guner, Y. Slimani, H. Gungunes, Md. Amir, A. Manikandan, A. Baykal, Microstructural, optical, and magnetic properties of vanadiumsubstituted nickel spinel nanoferrites, J. Supercond. Nov. Magn. 32 (2019) 1057–1065, https://doi.org/10.1007/s10948-018-4793-6.
- [66] Y. Slimani, M.A. Almessiere, S. Guner, N.A. Tashkandi, A. Baykal, M.F. Sarac, M. Nawaz, I. Ercan, Calcination effect on the magneto-optical properties of vanadium substituted NiFe<sub>2</sub>O<sub>4</sub> nanoferrites, J. Mater. Sci.: Mater. Electron. 30 (2019) 9143–9154, https://doi.org/10.1007/s10854-019-01243-x.

- [67] J. Tauc, R. Grigorovici, A. Vancu, Optical properties and electronic structure of amorphous germanium, Phys. Status Solidi B 15 (2) (1966) 627, https://doi.org/ 10.1002/pssb.19660150224.
- [68] S.N. Dolia, R. Sharma, M. Sharma, N. Saxena, Synthesis, X-ray diffraction and optical band gap study of nanoparticles of NiFe<sub>2</sub>O<sub>4</sub>, Indian J. Pure Appl. Phys. 44 (2006) 774–776, https://doi.org/10.1103/PhysRevB.86.205106.
- [69] Q. C. Sun, H. Sims, D. Mazumdar, J.X. Ma, B.S. Holinsworth, K.R. O'Neal, G. Kim, W.H. Butler, A. Gupta, J.L. Musfeldt, Optical band gap hierarchy in a magnetic oxide: electronic structure of NiFe<sub>2</sub>O<sub>4</sub>, Phys. Rev. B: Condens. Matter Mater. Phys. 86 (2012), 205106, https://doi.org/10.1103/PhysRevB.86.205106.
- [70] S. Balaji, R. Kalai Selvan, L. John Berchmans, S. Angappan, K. Subramanian, C. O. Augustin, Combustion synthesis and characterization of Sn<sup>4+</sup> substituted nanocrystalline NiFe<sub>2</sub>O<sub>4</sub>, Mater. Sci. Eng., B 119 (2005) 119–124, https://doi.org/10.1016/j.mseb.2005.01.021.
- [71] H. Yao, X. Ning, H. Zhao, A. Hao, M. Ismail, Effect of Gd-doping on structural, optical, and magnetic properties of NiFe<sub>2</sub>O<sub>4</sub> as-prepared thin films via facile sol–gel approach, ACS Omega 6 (2021) 6305–6311, https://doi.org/10.1021/acsomega.0c06097.
- [72] P. Priyadharshini, P.A. Shobika, P. Monisha, S.S. Gomathi, K. Pushpanathan, Nickel ferrite magnetic nanoparticles: evidence for superparamagnetism in smaller size particles, J. Aust. Ceram. Soc. 58 (2022) 1455–1480, https://doi.org/10.1007/ s41779-022-00784-5.
- [73] P. Chand, S. Vaish, P. Kumar, Structural, Optical and dielectric properties of transition metal (MFe<sub>2</sub>O<sub>4</sub>; M=Co,Ni and Zn) nanoferrites, Physica B 524 (2017) 53–63, https://doi.org/10.1016/j.physb.2017.08.060.
- [74] M. Hjíri, N.H. Alonizan, M.M. Althubayti, S. Alshammari, H. Besbes, M.S. Aida, Preparation, and photoluminescence of NiFe<sub>2</sub>O<sub>4</sub> nanoparticles, J. Mater. Sci.: Mater. Electron. 30 (2019) 15379–15387, https://doi.org/10.1007/s10854-019-01914-9
- [75] Y. Xia, Z. He, J. Su, B. Tang, K. Hu, Y. Lu, S. Sun, X. Li, Fabrication of magnetically separable NiFe<sub>2</sub>O<sub>4</sub>/BiOI nanocomposites with enhanced photocatalytic performance under visible-light irradiation, RSC Adv. 8 (2018) 4284–4294, https://doi.org/10.1039/C7RA12546A.
- [76] P. Monisha, P. Priyadharshini, S.S. Gomathi, M. Mahendran, K. Pushpanathan, Role of Zn dopant on superparamagnetic property of CoFe<sub>2</sub>O<sub>4</sub> nanoparticles, Appl. Phys. A 125 (2019) 736, https://doi.org/10.1007/s00339-019-3014-x.

- [77] P. Monisha, P. Priyadharshini, S.S. Gomathi, K. Pushpanathan, Influence of Mn dopant on the crystallite size, optical and magnetic behaviour of CoFe<sub>2</sub>O<sub>4</sub> magnetic nanoparticles, J. Phys. Chem. Solids 148 (2021), 109654, https://doi.org/10.1016/j.jpcs.2020.109654.
- [78] A. Hashhash, M. Kaiser, Influence of Ce-substitution on structural, magnetic, and electrical properties of cobalt ferrite nanoparticles, J. Electron. Mater. 45 (2016) 462–472, https://doi.org/10.1007/s11664-015-4125-6.
- [79] F. Kools, Reaction-induced grain growth impediment during sintering of strontium hexaferrite with silica addition, Solid State Ion 16 (1985) 251–259, https://doi. org/10.1016/0167-2738(85)90049-9.
- [80] D. Padalia, U.C. Johri, M.G.H. Zaidi, Effect of cerium substitution on structural and magnetic properties of magnetite nanoparticles, Mater. Chem. Phys. 169 (2016) 89–95, https://doi.org/10.1016/j.matchemphys.2015.11.034.
- [81] M.K. Anupama, N. Srinatha, S. Matteppanavar, B. Angadi, B Sahoo, B. Rudraswamy, Effect of Zn substitution on the structural and magnetic properties of nanocrystalline NiFe<sub>2</sub>O<sub>4</sub> ferrites, Ceram. Int. 44 (2018) 4946–4954, https://doi. org/10.1016/j.ceramint.2017.12.087.
- [82] E.C. Stoner, E.P. Wohlfarth, A mechanism of magnetic hysteresis in heterogeneous alloys, Philos. Trans. R. Soc. A 240 (826) (1948) 599–642, https://doi.org/ 10.1098/rsta.1948.0007.
- [83] S.D. Chhaya, M.P. Pandya, M.C. Chhantbar, K.B. Modi, G.J. Baldha, H.H. Joshi, Study of substitution limit, structural, bulk magnetic and electrical properties of Ca<sup>2+</sup> substituted magnesium ferrite, J. Alloys Compds. 377 (2004) 155–161, https://doi.org/10.1016/j.jallcom.2003.11.151.
- [84] V. Sepelak, I. Bergmann, A. Feldhoff, P. Heitjans, F. Krumeich, D. Menzel, F. J. Litterst, S.J. Campbell, K.D. Becker, Nanocrystalline nickel ferrite, NiFe<sub>2</sub>O<sub>4</sub> mechanosynthesis, nonequilibrium cation distribution, canted spin arrangement, and magnetic behavior, J. Phys. Chem. C 111 (2007) 5026, https://doi.org/10.1021/jp067620s.
- [85] K.V. Chandekar, K.M. Kant, Estimation of the spin-spin relaxation time of surfactant coated CoFe<sub>2</sub>O<sub>4</sub> nanoparticles by electron paramagnetic resonance spectroscopy, Phys. E: Low-Dimens. Syst. Nanostruct. 104 (2018) 192–205, https://doi.org/10.1016/j.physe.2018.06.016.
- [86] V.J. Angadi, B. Rudraswamy, K. Sadhana, S.R. Murthy, K. Praveena, Effect of Sm<sup>3</sup> +Gd<sup>3+</sup> on structural, electrical and magnetic properties of Mn–Zn ferrites synthesized via combustion route, J. Alloys Compd. 656 (2016) 5–12, https://doi.org/10.1016/j.jallcom.2015.09.222.